Journal of Computational Chemistry

WILEY

Journal of COMPUTATIONAL CHEMISTRY

RESEARCH ARTICLE

Simplified Time-Dependent DFT for all-Atom Simulations of Second Harmonic Generation Responses: A Case Study on Photoswitchable Azobenzene Monolayers

Matt Hugget[1] | Angela Dellai[1,2] | Philippe Aurel[1] | Marilù G. Maraldi[3] | Marc de Wergifosse[3] | Frédéric Castet[1]

[1]Institut des Sciences Moléculaires, UMR 5255, Univ. Bordeaux, CNRS, Bordeaux INP, Talence, France | [2]CEISAM, UMR CNRS 6230, Nantes Université, Nantes, France | [3]Theoretical Chemistry Group, Molecular Chemistry Materials and Catalysis Division (MOST), Institute of Condensed Matter and Nanosciences, Université Catholique de Louvain, Louvain-la-Neuve, Belgium

Correspondence: Marc de Wergifosse (marc.dewergifosse@uclouvain.be) | Frédéric Castet (frederic.castet@u-bordeaux.fr)

Received: 13 January 2026 | **Revised:** 13 January 2026 | **Accepted:** 28 January 2026

Keywords: azobenzene | nonlinear optics | photoswitches | simplified TDDFT | TDDFT

ABSTRACT

Predicting the nonlinear optical (NLO) properties of large, disordered supramolecular aggregates is challenging because fully capturing dynamic fluctuations and intermolecular interactions requires a quantum-mechanical treatment of aggregation effects that remains out of reach for conventional computational methods. In the simplified time-dependent density functional theory (sTD-DFT) framework, we present a fully automated protocol for optimally tuning the Mataga-Nishimoto-Ohno-Klopman (MNOK) expressions of the two-electron integrals, enabling the prediction of NLO responses at a fraction of the cost of conventional TD-DFT. Using ground-state molecular orbitals from either DFT or extended tight-binding (xTB) calculations, the transferability of the optimized parameters is validated across isolated molecules, small model aggregates, and supramolecular clusters representative of azobenzene self-assembled monolayers (SAMs) extracted from molecular dynamics (MD) simulations. The results show that sTD-DFT reliably reproduces TD-DFT NLO responses and allows the treatment of large, disordered aggregates. Comparison of cluster- and fragment-based NLO responses shows that aggregation significantly reduces the second-harmonic generation (SHG) signal in azobenzene SAMs. Furthermore, comparing full sTD-DFT calculations with those relying on an electrostatic embedding of the environment reveals that both the *trans*/*cis* NLO contrast and the anisotropy of the SHG responses can differ substantially when all molecules are treated on an equal quantum-mechanical footing. These results demonstrate that combining MD simulations with optimally tuned sTD-DFT provides a practical strategy for evaluating NLO responses in complex supramolecular systems, fully capturing aggregation effects at an all-atom quantum mechanical (AQM) level.

1 | Introduction

The rational design of photoresponsive 2D materials capable of remote and reversible commutation of optical properties is a central challenge for the development of next-generation photonic devices. In particular, surface functionalized by self-assembled monolayers (SAMs) incorporating nonlinear optical (NLO) molecular switches, where the second harmonic generation (SHG) response serves as a probe of the conformational state of the molecular units, provide a non-destructive strategy for information readout [1–5]. This advantage arises from the use of near-infrared excitation wavelengths in SHG, which are insufficient in energy to trigger uncontrolled photoconversions or competing side reactions. Beyond surface engineering, the rational design of such materials and the optimization of their performance critically rely on computational approaches that provide

Abbreviations: AZO, azobenzene; MD, molecular dynamics; QM, quantum mechanics.

a microscopic description of interfacial molecular organization and establish predictive links to their NLO responses.

However, accurately modeling the NLO properties of supramolecular systems represents a major challenge for computational chemistry, as it requires addressing two key aspects: (i) The influence of dynamic effects, such as thermally induced structural fluctuations, and (ii) the impact of the environment [6]. A common strategy to account for dynamic effects is to couple molecular dynamics (MD) simulations with subsequent quantum mechanical (QM) calculations (most often based on time-dependent density functional theory, TD-DFT) on representative molecular snapshots extracted from the MD trajectories [7–13]. This approach has been successfully applied to compute the NLO responses of organic dyes in solution [14–18], but also to more complex systems such as dye-functionalized lipid bilayers [19–24], SAMs [3–5], organic aggregates in solution [25, 26] and alcohol/air interfaces [27, 28].

The treatment of environment effects can be carried out using a variety of methods, ranging from implicit solvation approaches such as the polarizable continuum model (PCM) to more elaborate hybrid schemes such as QM/MM or QM/QM [29, 30]. These latter frameworks rely on partitioning the system into a central region, which largely determines the NLO response and is treated at a high level of theory, and a peripheral region, which is assumed to play a secondary role and can therefore be described with a more approximate level of theory. When combined with polarizable force fields, such methods can capture both electrostatic and mutual polarization between the central region and its environment, and have been shown to perform well for systems where the surrounding medium has a weak intrinsic NLO response [30, 31].

However, QM/MM and QM/QM approaches reach their limits when applied to supramolecular clusters such as nanoparticles or SAMs, in which all molecular units are expected to contribute significantly to the overall NLO response. In these cases, the distinction between central and peripheral regions may become artificial. Despite this limitation, hybrid schemes have been employed by some of us to investigate the NLO properties of photoresponsive SAMs composed of azobenzene (AZO) photoswitches [4, 5]. In these studies, MD simulations were first used to determine the morphology of the SAMs in both their *trans* and *cis* configurations. Subsequent TD-DFT calculations of the NLO responses were performed on isolated molecular fragments extracted from the SAM, with electrostatic intermolecular interactions included through point-charge embeddings (PCEs) positioned at the atomic coordinates of neighboring molecular fragments. These calculations were repeated for all constituent chromophores across multiple time frames, thereby providing both temporal and spatial sampling of the molecular NLO responses. Nevertheless, this approach suffers from significant shortcomings, as it neglects mutual (self-consistent) polarization effects and the possibility of delocalized excited states, while both of which can have a critical influence on the overall NLO response. Therefore, a full QM treatment of large supramolecular aggregates, in which all constituent molecules are treated on an equal footing, remains necessary for achieving predictive accuracy.

However, TD-DFT calculations rapidly become computationally prohibitive as the system size increases, restricting their applicability to small aggregates containing only a few molecules. In this context, a promising and cost-effective alternative is offered by simplified TD-DFT (sTD-DFT) schemes [32–37]. These methods can be applied to systems comprising thousands of atoms, allowing the explicit inclusion of aggregation effects such as mutual polarization and intermolecular electronic couplings. Compared to standard TD-DFT, sTD-DFT relies on a set of approximations, including simplified and parameterized expressions for the two-electron integrals, truncation of the configuration state function (CSF) space, and neglect of terms involving the response of the exchange-correlation potential in Casida equations. Despite its simplicity, the reliability of sTD-DFT has been demonstrated for the calculation of NLO responses in diverse systems, ranging from push-pull π-conjugated compounds to fluorescent proteins and collagen [38–41]. It has also been successfully employed to rationalize the SHG responses of amorphous nanoparticles formed by organic dipolar dyes in water [25].

Like any semi-empirical approach, sTD-DFT fundamentally inherits the accuracy of the reference method used for its parameterization, while still requiring system-specific calibration and careful benchmarking for the targeted properties. In most previous studies, sTD-DFT has been parameterized to reproduce excited-state energies, whereas a few dedicated parameterizations have been developed to describe NLO properties [25, 38, 39]. In this work, we apply an optimally-tuned sTD-DFT approach to investigate the NLO responses of AZO monolayers, extending our previous studies [4, 5] based on MD-generated structures by enabling all-atom quantum mechanical (AQM) calculations of their SHG responses. For reliable results, the parameterization must reproduce the SHG response of both equilibrium and distorted molecular subunits extracted from MD trajectories, where steric constraints in the SAM lead to significant deviations from ground-state geometries. Moreover, because supramolecular systems are targeted, the sTD-DFT scheme must reliably capture environment effects on the SHG response. Finally, for practical applicability, the parameterization procedure itself should remain as straightforward as possible.

In the first part of this study, we develop a simple, fully automated, protocol for parameterizing the approximated expressions of the two-electron integrals within the sTD-DFT framework. The quality of the parameterization is assessed by comparing sTD-DFT predictions of the NLO responses of isolated molecules and small model aggregates with reference TD-DFT results. The choice of the ground-state molecular orbitals (MOs), used as an input for the sTD-DFT scheme, is also discussed. In the second part, the optimally-tuned sTD-DFT scheme is applied to compute the SHG response of large aggregates representative of AZO monolayers, thereby capturing all relevant aggregation effects.

2 | Systems, Properties, and Computational Approaches

2.1 | Investigated Systems

The sTD-DFT scheme is first parameterized to compute the SHG responses of the *cis* and *trans* isomers of a series of AZO derivatives (**1**–**9**, Figure 1a), which were recently synthesized and experimentally characterized by hyper-Rayleigh scattering

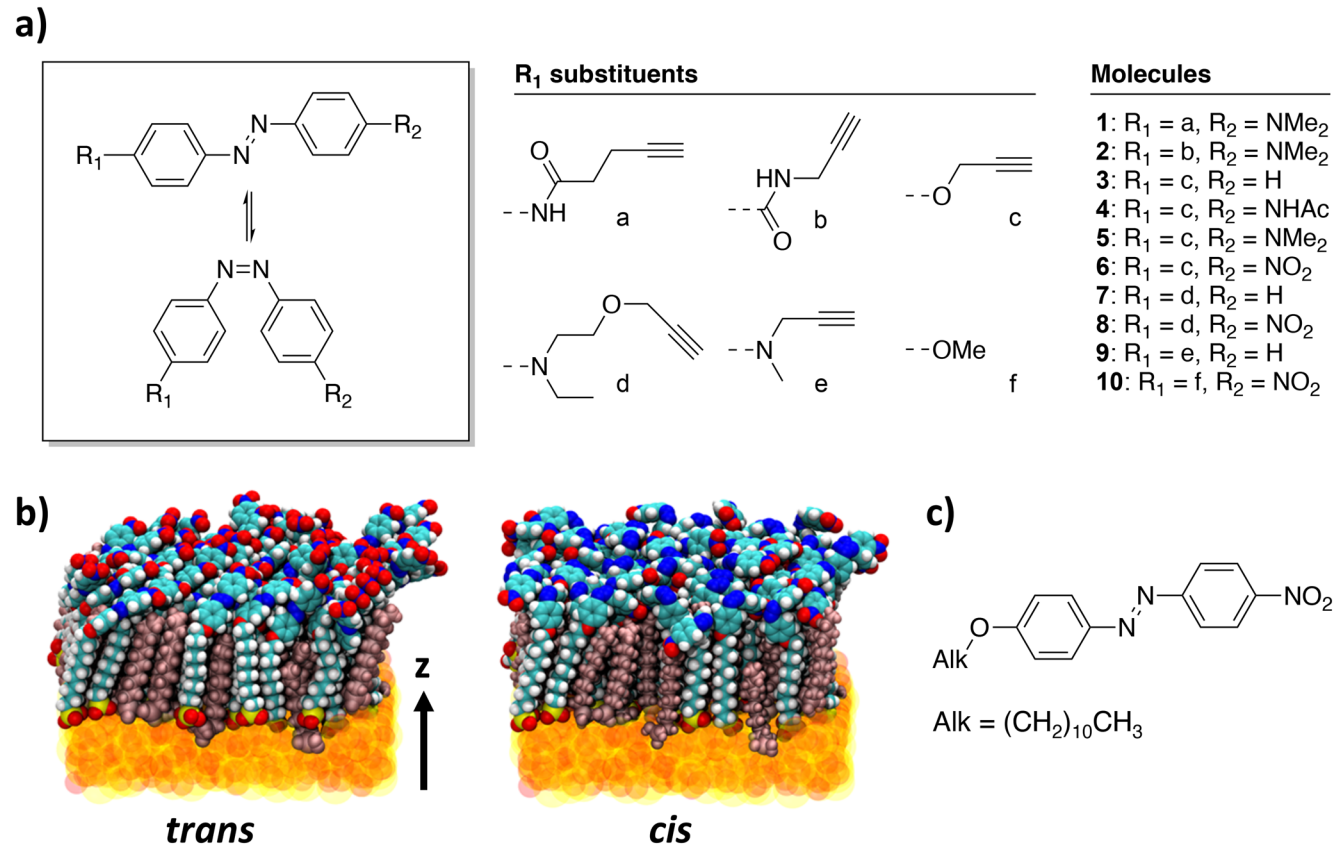

FIGURE 1 | (a) Structure of the surface-clickable azobenzene derivatives. (b) Lateral views of *trans* and *cis* SAMs as extracted from MD trajectories, see Reference [5], with in yellow the mobile section of the SiO_2 substrate and in brown the non functionalized alkyl chains. (c) Chemical structure of alkyl chains functionalized with a photoswitchable azobenzene core used in the SAMs.

(HRS) [42]. These compounds incorporate a clickable alkyne unit attached in para position to the AZO core via different linkers (R_1), while the phenyl ring on the opposite side is either unsubstituted or para-substituted (R_2) with electron-donating (–NHAc, $–NMe_2$) or electron-withdrawing ($–NO_2$) groups. In addition, compound **10**, bearing R_1 = OMe and $R_2 = NO_2$ and representative of the photochromic units used in the monolayers, is employed to further investigate the influence of intermolecular interactions on the first hyperpolarizability in model molecular dimers.

In the second part, the sTD-DFT scheme, calibrated with the optimal parameters determined for compound **10**, is applied to compute the SHG responses of molecular fragments extracted from MD trajectories of the SAMs depicted in Figure 1b. These MD simulations were reported in our previous work [5]. The simulation box for the investigated SAMs contains 121 densely packed dodecylsilyl chains with a functionalization ratio of 50%: AZO units are grafted onto 61 of the 121 alkyl chains, while the remaining 60 chains remain non-functionalized. Practically, 10 frames were selected from the production runs of both *trans* and *cis* SAMs. From each frame, the 61 functionalized molecular residues shown in Figure 1c were isolated, resulting in 610 geometries for each conformation. Note that, owing to the incomplete photoisomerization yield (95%) [5], three AZO units remain in the *trans* configuration within the nominally *cis* SAM. Comparison of the SHG responses predicted by sTD-DFT with those obtained using standard TD-DFT for this ensemble of geometries enables assessing the robustness of the parameterization against the geometrical distortions experienced by the molecules within the SAMs. Finally, sTD-DFT calculations were carried out on increasingly large molecular clusters extracted from the MD morphologies of the *trans* and *cis* SAMs (including both AZO-functionalized and non functionalized alkyl chains), to investigate aggregation effects on the SHG responses.

2.2 | Second-Order NLO Responses

The NLO responses investigated herein are related to the SHG process. The 18 independent components of the dynamic (frequency-dependent) first hyperpolarizability tensor $\beta(-2\omega;\omega,\omega) = \beta^{\omega}$ were calculated for AZO derivatives in their equilibrium geometry, as well as for individual AZO residues or AZO clusters extracted from MD trajectories. NLO responses were calculated using specific incident wavelengths $\lambda_{inc} = 2\pi c/\omega$, as well as in the static (infinite wavelength) limit ($\omega = 0$).

For isolated molecules, first hyperpolarizabilities related to HRS experiments, β_{HRS}, were evaluated. β_{HRS} is expressed as the sum of two contributions associated to vertical (V) or horizontal (H) polarization of the incident beam in the laboratory frame, while the scattered light is assumed to be V-polarized:

$$\beta_{HRS}(-2\omega;\omega,\omega) = \sqrt{\langle \beta_{VV}^2 \rangle + \langle \beta_{HV}^2 \rangle} \quad (1)$$

$\langle \beta^2_{VV} \rangle$ and $\langle \beta^2_{HV} \rangle$ are macroscopic averages of the molecular β tensor components [43].

$$\begin{aligned}\langle \beta^2_{VV} \rangle &= \frac{1}{7}\sum_{\zeta}^{x,y,z}\beta^2_{\zeta\zeta\zeta} + \frac{4}{35}\sum_{\zeta\neq\eta}^{x,y,z}\beta^2_{\zeta\zeta\eta} + \frac{2}{35}\sum_{\zeta\neq\eta}^{x,y,z}\beta_{\zeta\zeta\zeta}\beta_{\zeta\eta\eta} \\ &+ \frac{4}{35}\sum_{\zeta\neq\eta}^{x,y,z}\beta_{\eta\zeta\zeta}\beta_{\zeta\zeta\eta} + \frac{4}{35}\sum_{\zeta\neq\eta}^{x,y,z}\beta_{\zeta\zeta\zeta}\beta_{\eta\eta\zeta} + \frac{1}{35}\sum_{\zeta\neq\eta}^{x,y,z}\beta^2_{\eta\zeta\zeta} \\ &+ \frac{4}{105}\sum_{\zeta\neq\eta\neq\xi}^{x,y,z}\beta_{\zeta\zeta\eta}\beta_{\eta\xi\xi} + \frac{1}{105}\sum_{\zeta\neq\eta\neq\xi}^{x,y,z}\beta_{\eta\zeta\zeta}\beta_{\eta\xi\xi} \\ &+ \frac{4}{105}\sum_{\zeta\neq\eta\neq\xi}^{x,y,z}\beta_{\zeta\zeta\eta}\beta_{\xi\xi\eta} \\ &+ \frac{2}{105}\sum_{\zeta\neq\eta\neq\xi}^{x,y,z}\beta^2_{\zeta\eta\xi} + \frac{4}{105}\sum_{\zeta\neq\eta\neq\xi}^{x,y,z}\beta_{\zeta\eta\xi}\beta_{\eta\zeta\xi}\end{aligned} \tag{2}$$

$$\begin{aligned}\langle \beta^2_{HV} \rangle &= \frac{1}{35}\sum_{\zeta}^{x,y,z}\beta^2_{\zeta\zeta\zeta} + \frac{4}{105}\sum_{\zeta\neq\eta}^{x,y,z}\beta_{\zeta\zeta\zeta}\beta_{\zeta\eta\eta} - \frac{2}{35}\sum_{\zeta\neq\eta}^{x,y,z}\beta_{\zeta\zeta\zeta}\beta_{\eta\eta\zeta} \\ &+ \frac{8}{105}\sum_{\zeta\neq\eta}^{x,y,z}\beta^2_{\zeta\zeta\eta} + \frac{3}{35}\sum_{\zeta\neq\eta}^{x,y,z}\beta^2_{\zeta\eta\eta} - \frac{2}{35}\sum_{\zeta\neq\eta}^{x,y,z}\beta_{\zeta\zeta\eta}\beta_{\eta\zeta\zeta} \\ &+ \frac{1}{35}\sum_{\zeta\neq\eta\neq\xi}^{x,y,z}\beta_{\zeta\eta\eta}\beta_{\zeta\xi\xi} - \frac{2}{105}\sum_{\zeta\neq\eta\neq\xi}^{x,y,z}\beta_{\zeta\zeta\xi}\beta_{\eta\eta\xi} \\ &- \frac{2}{105}\sum_{\zeta\neq\eta\neq\xi}^{x,y,z}\beta_{\zeta\zeta\eta}\beta_{\eta\xi\xi} \\ &+ \frac{2}{35}\sum_{\zeta\neq\eta\neq\xi}^{x,y,z}\beta^2_{\zeta\eta\xi} - \frac{2}{105}\sum_{\zeta\neq\eta\neq\xi}^{x,y,z}\beta_{\zeta\eta\xi}\beta_{\eta\zeta\xi}.\end{aligned} \tag{3}$$

The $\langle \beta^2_{VV} \rangle / \langle \beta^2_{HV} \rangle$ ratio, referred to as the depolarization ratio (DR), was also evaluated as an indicator of the octupolar/dipolar symmetry of the NLO response.

For AZO residues or clusters representative of SAMs, the components and norm of the first hyperpolarizability vector were calculated as follows:

$$\beta_i = \frac{1}{3}\sum_j (\beta_{ijj} + \beta_{jij} + \beta_{jji}) \tag{4}$$

$$\beta = \sqrt{\beta_x^2 + \beta_y^2 + \beta_z^2} \tag{5}$$

where $i,j = x,y,z$ are the Cartesian axes, with (x,y) the surface plane and z the axis normal to the surface (see Figure 1). The anisotropy a_β of the NLO response was also evaluated, as the ratio between the hyperpolarizability vector components normal and parallel to the surface:

$$a_\beta = \frac{|\beta_z|}{\sqrt{\beta_x^2 + \beta_y^2}}. \tag{6}$$

NLO responses were computed either from equilibrium structures optimized at the DFT level or from statistical ensembles of geometries generated by MD simulations. In the latter case, mean values and standard deviations were extracted from the distributions obtained through the sequential MD+QM procedure. The standard deviation reflects the fluctuations of the computed property over time, arising from geometrical variations. It is directly connected to the spectral broadening of the responses and is associated with the statistical error of the mean by a factor of $1/\sqrt{N}$, where N is the number of sampled configurations [7, 44, 45]. All β values reported hereafter are given in atomic units (1 a.u. of $\beta = 3.6310^{-42}\mathrm{m^4V^{-1}} = 3.2063\times10^{-53}\mathrm{C^3m^3J^{-2}} = 8.641\times10^{-33}$ esu) according to the T convention [46].

2.3 | Basics of the sTD-DFT Method

In the following, the i,j,k,l indices label occupied MOs, and a,b,c,d unoccupied ones; p,q,r,s indices refer to the general case, where MOs can be either occupied or unoccupied. Within the standard TD-DFT framework, and under the singlet-restricted formalism using real orbitals, the Casida equations are given by:

$$\left[\begin{pmatrix}\boldsymbol{A} & \boldsymbol{B}\\ \boldsymbol{B} & \boldsymbol{A}\end{pmatrix} - \omega\begin{pmatrix}1 & 0\\ 0 & -1\end{pmatrix}\right]\begin{pmatrix}\boldsymbol{X}_\zeta(\omega)\\ \boldsymbol{Y}_\zeta(\omega)\end{pmatrix} = -\begin{pmatrix}\boldsymbol{\mu}_\zeta\\ \boldsymbol{\mu}_\zeta\end{pmatrix} \tag{7}$$

where the vector $\boldsymbol{\mu}_\zeta$ has for elements $\mu_{\zeta,ia} = \langle i|\hat{\mu}_\zeta|a\rangle$ in which $\hat{\mu}_\zeta$ is the ζ-component of the dipole operator, ω the frequency of the external electric field, and $\boldsymbol{X}_\zeta(\omega)$ and $\boldsymbol{Y}_\zeta(\omega)$ the frequency-dependent excitation and de-excitation response vectors, respectively. For global hybrid exchange-correlation functionals (XCFs), the elements of the $\boldsymbol{A}$ and $\boldsymbol{B}$ supermatrices are expressed as:

$$\begin{aligned}A_{ia,jb} &= \delta_{ij}\delta_{ab}(\epsilon_a - \epsilon_i) + 2(ia|jb) - a_x(ij|ab) + (1-a_x)(ia|f_{XC}|jb)\\ B_{ia,jb} &= 2(ia|bj) - a_x(ib|aj) + (1-a_x)(ia|f_{XC}|bj)\end{aligned} \tag{8}$$

where a_x is the amount of Hartree-Fock (HF) exchange in the XCF and ϵ_p is the energy of the p orbital. The integrals $(ia|jb)$, $(ia|bj)$ and $(ib|aj)$ are exchange-type, $(ij|ab)$ are Coulomb-type, and $(ia|f_{XC}|jb)$ and $(ia|f_{XC}|bj)$ are the responses of the exchange correlation kernel f_{XC}. The frequency-dependent linear response vectors are obtained as:

$$\left[(\boldsymbol{A}+\boldsymbol{B}) - \omega^2(\boldsymbol{A}-\boldsymbol{B})^{-1}\right]\left[\boldsymbol{X}_\zeta(\omega) + \boldsymbol{Y}_\zeta(\omega)\right] = -2\boldsymbol{\mu}_\zeta \tag{9}$$

In the case of SHG, the elements of the β tensor are then computed as:

$$\beta_{\xi\zeta\eta}(-2\omega;\omega,\omega) = A - B + C \tag{10}$$

with:

$$A = \sum_{perm.\xi,\zeta,\eta}\left\{\sum_{aij}X_{\xi,ai}(-2\omega)\left[-\mu_{\zeta,ij} + \sum_{ck}f^{HXC}_{ij,ck}\left(X_{\zeta,ck}(\omega) + Y_{\zeta,ck}(\omega)\right)\right]Y_{\eta,aj}(\omega)\right\} \tag{11}$$

$$B = \sum_{perm.\xi,\zeta,\eta}\left\{\sum_{iab}X_{\xi,ai}(-2\omega)\left[-\mu_{\zeta,ab} + \sum_{ck}f^{HXC}_{ab,ck}\left(X_{\zeta,ck}(\omega) + Y_{\zeta,ck}(\omega)\right)\right]Y_{\eta,bi}(\omega)\right\} \tag{12}$$

$$C = \sum_{perm.\xi,\zeta,\eta} \left\{ \sum_{aibjck} g^{XC}_{ai,bj,ck} \left[X_{\xi,ai}(-2\omega) + Y_{\xi,ai}(-2\omega)\right] \left[X_{\zeta,bj}(\omega) + Y_{\zeta,bj}(\omega)\right] \left[X_{\eta,ck}(\omega) + Y_{\eta,ck}(\omega)\right] \right\} \quad (13)$$

where $\sum_{perm.\xi,\zeta,\eta}$ runs over six different permutations of $\{\xi,\zeta,\eta\}$ directions, $g^{XC}_{ai,bj,ck}$ are matrix elements of the third-order derivative of the XCF, and $f^{HXC}_{ij,ck}$ are the elements of the Hartree exchange-correlation (HXC) kernel defined as:

$$f^{HXC}_{ij,ck} = 2(ij|ck) - a_x(jk|ci) + (1-a_x)(ij|f_{XC}|ck) \quad (14)$$

Within the sTD-DFT scheme, three approximations are introduced [37, 47]. First, all f_{XC} dependent contributions in Equation (8) are neglected, resulting in simplified supermatrix elements:

$$\begin{aligned} A'_{ia,jb} &= \delta_{ij}\delta_{ab}(\epsilon_a - \epsilon_i) + 2(ia|jb)' - a_x(ij|ab)' \\ B'_{ia,jb} &= 2(ia|bj)' - a_x(ib|aj)' \end{aligned} \quad (15)$$

and the linear response vectors are expressed similarly as in Equation (9):

$$\left[\left(\boldsymbol{A}' + \boldsymbol{B}'\right) - \omega^2\left(\boldsymbol{A}' - \boldsymbol{B}'\right)^{-1}\right]\left[\boldsymbol{X}'_\zeta(\omega) + \boldsymbol{Y}'_\zeta(\omega)\right] = -2\boldsymbol{\mu}_\zeta. \quad (16)$$

Second, the configuration interaction (CI) space is truncated, so that only a selected subset of single excitations is retained based on an energy threshold, which defines the spectral range for an excited state calculation. Third, the two-electron integrals $(pq|rs)'$ are approximated by using the zero differential overlap (ZDO) approximation based on Löwdin orthogonalized (LO) orbitals, retaining only one- and two-center terms, and are expressed as follows:

$$(pq|rs)' = \sum_A^N \sum_B^N Q^A_{pq} Q^B_{rs} (AA|BB) \quad (17)$$

where Q^A_{pq} and Q^B_{rs} are charge densities localized on atoms A and B respectively, computed from LCAO coefficients in the LO space. The $(AA|BB)$ factor is the Mataga-Nishimoto-Ohno-Klopman (MNOK) damped Coulomb integral [48–50], which takes slightly different forms for Coulomb (J) and exchange (K):

$$a_x(AA|BB)^J = \left(\frac{1}{(R_{AB})^{\gamma_J} + (a_x\eta)^{-\gamma_J}}\right)^{\frac{1}{\gamma_J}} \quad (18)$$

$$(AA|BB)^K = \left(\frac{1}{(R_{AB})^{\gamma_K} + \eta^{-\gamma_K}}\right)^{\frac{1}{\gamma_K}} \quad (19)$$

where R_{AB} is the interatomic distance between atoms A and B, and η is the mean chemical hardness of the two atoms [51]. The exponents γ_J and γ_K are adjustable parameters optimized to reproduce targeted optical property (in this work the first hyperpolarizability) of the investigated system relative to reference calculations. Finally, within the quadratic response sTD-DFT scheme, two extra simplifications are made: The C term is omitted in Equation (10), and all terms containing the HXC kernel are neglected in Equations (11) and (12). The expression of the first hyperpolarizability components thus reduces as:

$$\beta'_{\xi\zeta\eta}(-2\omega;\omega,\omega) = A' - B' \quad (20)$$

with:

$$A' = \sum_{perm.\xi,\zeta,\eta} \left\{ \sum_{aij} X'_{\xi,ai}(-2\omega)\left[-\mu_{\zeta,ij}\right] Y'_{\eta,aj}(\omega) \right\} \quad (21)$$

$$B' = \sum_{perm.\xi,\zeta,\eta} \left\{ \sum_{iab} X'_{\xi,ai}(-2\omega)\left[-\mu_{\zeta,ab}\right] Y'_{\eta,bi}(\omega) \right\}. \quad (22)$$

Overall, the sTD-DFT approach relies on a set of input parameters that can be adjusted according to the system under study. These include the fraction of exact HF exchange a_x, the energy threshold defining the CI space (E_{thr}), and the exponents γ_J and γ_K of the MNOK two-electron integrals. In all sTD-DFT calculations reported here, an energy threshold of 7 eV was employed, as it provides a good compromise between accuracy and computational cost for reproducing the NLO response of isolated molecules (see Figures S1 and S2). The amount of HF exchange was set according to the TD-DFT reference XCF used for parameterizing γ_J and γ_K (see next section); for the M06-2X functional, $a_x = 0.54$.

The ground-state MOs must also be generated beforehand and provided as input for the sTD-DFT calculations in order to construct the $\boldsymbol{A}'$ and $\boldsymbol{B}'$ supermatrices. In this work, for the sake of consistency, the ground state MOs used in all sTD-DFT calculations are identical to those used for optimizing the $\{\gamma_J, \gamma_K\}$ parameters. However, this approach (referred to as sTD-DFT[DFT] hereafter), becomes computationally demanding for large systems. Alternatively, tight-binding-based calculations [52] offer a much more economical option for generating the ground state MOs, albeit with a possible loss of accuracy. This approach is hereafter referred to as sTD-DFT[xTB], where xTB stands for extended tight-binding [52].

2.4 | General Protocol for sTD-DFT Parameterization

The computational protocol developed in this work for the parameterization of the two-electron integrals of the sTD-DFT method and its validation against regular TD-DFT calculations is illustrated in Figure 2. The first step consists in computing the system's geometry and its ground state MOs. The geometries of isolated molecules were optimized using DFT at the ωB97X-D/6-311G(d) level of theory (M06-2X/6-311G(d) for molecule **10**), while their electronic structures were evaluated using M06-2X with the more extended 6-311+G(d) basis set, which includes additional diffuse functions.

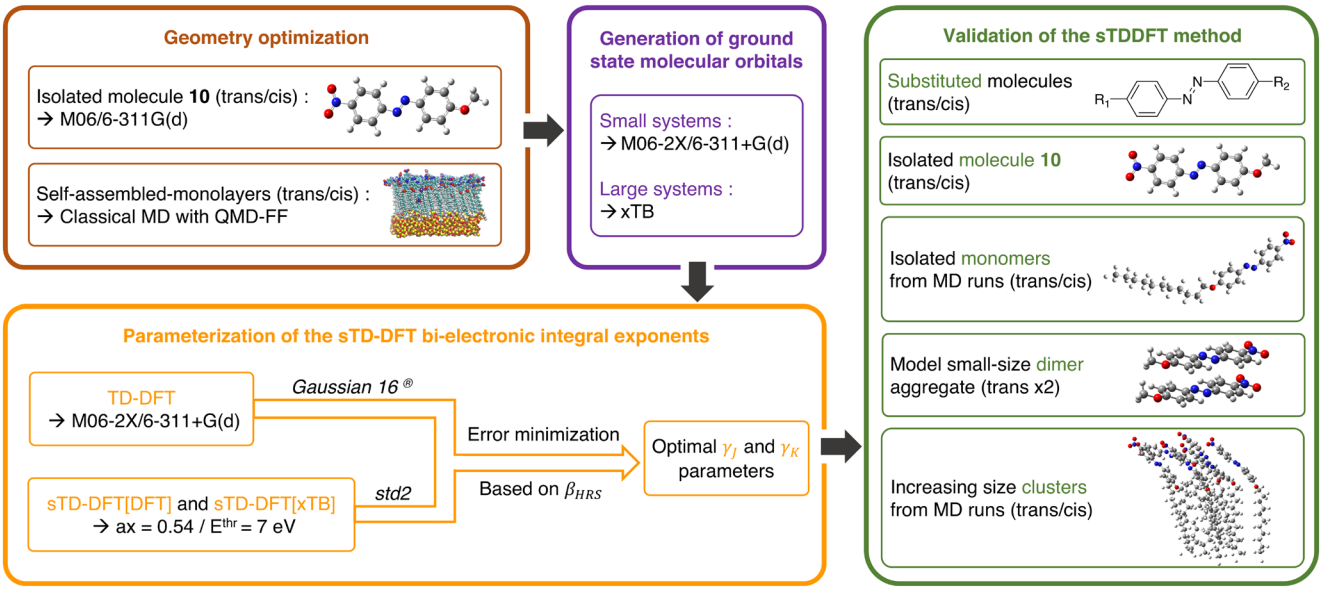

FIGURE 2 | Computational protocol for the parameterization of the sTD-DFT method and its subsequent use for the calculation of second harmonic responses of large supramolecular aggregates at a full quantum level.

The geometries of supramolecular aggregates were extracted from MD simulations employing quantum-mechanics-derived force fields (QMD-FFs), as reported in Reference [5]. The MOs of these aggregates were computed at the M06-2X level with the 6-311+G(d) basis set, or with the smaller 6-31G(d) basis set when the computational cost was prohibitive. For the largest clusters, the MOs were obtained using the xTB method [52]. In all DFT calculations, Cartesian atomic orbitals have been used together with tight (σ_r, σ_a) integration grids (with σ_r the number of radial shells and σ_a the angular points per shell), to ensure the accuracy of the electronic density. The (175, 974) grid was used for hydrogen, while the (250, 974) grid was used for other atoms.

In a second step, the brute-force parameterization of the γ_J and γ_K parameters in Equations (18) and (19) was carried out on isolated AZO molecules in their equilibrium geometry by generating two-dimensional error maps, minimizing the deviation of the HRS hyperpolarizability with respect to reference TD-DFT calculations. These latter were carried out at the M06-2X/6-311+G(d) level, which has been shown in previous studies to provide reliable accuracy for second-order NLO properties of organic dyes [53, 54]. For molecule **10**, the sTD-DFT[DFT] scheme was also parameterized based on reference TD-DFT calculations carried out using the CAM-B3LYP range-separated hybrid functional with the 6-311+G(d) basis set. These results are reported and discussed in SI (Table S3).

Importantly, a single set of $\{\gamma_J, \gamma_K\}$ parameters was enforced for both *trans* and *cis* isomers, since the molecular geometries sampled from MD simulations deviate from equilibrium and often correspond to intermediate conformations between the two forms. For consistency, identical parameters must therefore be used within a given molecular system and optimized with respect to the mean β_{HRS} value of both isomers. In addition, it is crucial to avoid situations where one isomer exhibits a very small error while the other shows a large one, as this would strongly bias the $\beta_{HRS}(trans)/\beta_{HRS}(cis)$ contrast, which is an important indicator of the efficiency of switchable NLO systems. To address this, the standard deviation of β_{HRS} values is also taken into account for determining the optimal $\{\gamma_J, \gamma_K\}$ parameters, as detailed in the Section S1.2. Finally, as discussed below, parameterization can either be performed at a specific incident wavelength, or achieved by reproducing the full dispersion profile of the first hyperpolarizability over a given spectral range.

In a third step, the transferability of the optimally tuned parameters is assessed against reference TD-DFT calculations for different test cases: (i) Model molecular pairs with both molecules in their equilibrium *trans* geometry, (ii) isolated molecular fragments and (iii) supramolecular aggregates, both extracted from MD simulations. Once validated, the parameterized sTD-DFT scheme can be applied to predict the NLO responses of large aggregates that are beyond the practical scope of standard TD-DFT calculations, while providing a reliable estimate of the error with respect to the reference method.

All the reported DFT and TD-DFT calculations were carried out using the `Gaussian 16` program [55], while xTB and sTD-DFT calculations were performed with the `xtb4stda` [56] and `std2` [57] codes, respectively.

3 | Results and Discussion

3.1 | Parameterization and Validation of the sTD-DFT Scheme

3.1.1 | Derivatives With Different Substitution Patterns

In this section, we assess the reliability of the optimally-tuned sTD-DFT[DFT] scheme in reproducing dynamic ($\lambda_{inc} = 1064$ nm) HRS hyperpolarizability values calculated at the reference TD-DFT/M06-2X/6-311+G(d) level for the series of compounds shown in Figure 1a. The $\{\gamma_J, \gamma_K\}$ parameters of the two-electron integrals (Equations (18) and (19)) were optimized following the procedure described in Section 2.4 (see also details

in Section S1.2), imposing a single parameter set for both *trans* and *cis* forms to ensure robustness toward dynamic structural fluctuations and non-equilibrium conformations. Note also that molecules **1**, **2**, and **4** each exhibit two distinct conformers (labeled **c1** and **c2**), which differ by the orientation of the R_1 or R_2 substituent (Figure S3). For these compounds, the parameterization procedure was carried out by imposing the same $\{\gamma_J, \gamma_K\}$ parameters for both conformers.

In practice, 2D maps showing how the sTD-DFT dynamic ($\lambda_{inc} = 1064$ nm) HRS hyperpolarizability (β^{ω}_{HRS}) deviates from the reference TD-DFT values as a function of the γ_J and γ_K parameters were generated for all AZO derivatives in their *trans* and *cis* forms. The parameters were varied from 0.05 to 5.0 in increments of 0.05, as illustrated in Figure 3 for molecule **10**. From these maps, a single optimal parameter set applicable to both forms was identified; for molecule **10**, $\{\gamma_J, \gamma_K\}_{opt} = \{0.95, 1.15\}$, yielding relative absolute errors (RAEs) of 1.77% and 1.92% for the *cis* and *trans* isomers, respectively.

The values of the optimal $\{\gamma_J, \gamma_K\}_{opt}$ parameters determined using the same procedure for molecules **1**-**10** are reported in Table S1. The wide spread of the parameter values, in particular γ_K, indicates a strong system dependence. Moreover, they differ substantially from those optimized to reproduce excitation energies in small and π-conjugated molecules ($\{\gamma_J, \gamma_K\} = \{1.94, 1.68\}$ for M06-2X) [32], highlighting the need for property-specific parameterization within the sTD-DFT framework.

The deviation on the β^{ω}_{HRS} values computed using the optimally-tuned sTD-DFT scheme with respect to reference TD-DFT/M06-2X/6-311+G(d) calculations is illustrated in Figure 4. Note

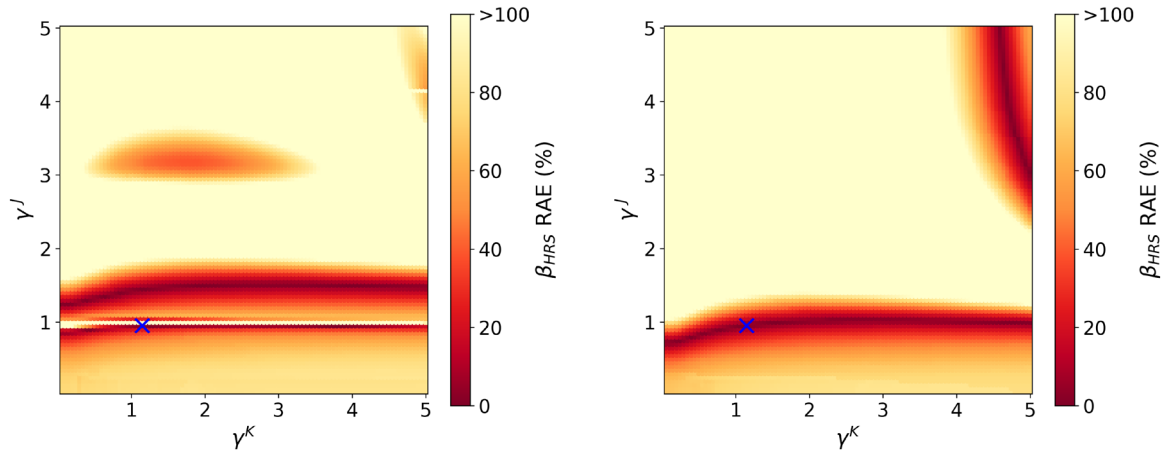

FIGURE 3 | sTDDFT[DFT] RAE on β^{ω}_{HRS} ($\lambda_{inc} = 1064$ nm) for the *cis* (left) and *trans* (right) forms of molecule **10**, with respect to TD-DFT calculations carried out at the M06-2X/6-311+G(d) level. The set of optimal parameters applicable to both *trans* and *cis* forms ($\{\gamma_J, \gamma_K\}_{opt} = \{0.950, 1.150\}$) is marked with a blue cross.

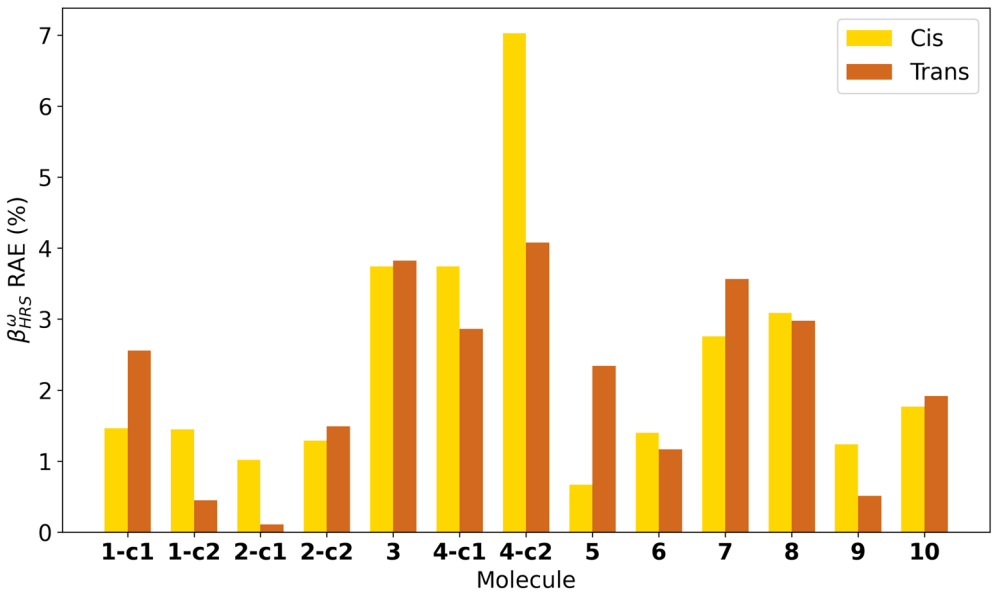

FIGURE 4 | Deviation (%) of β^{ω}_{HRS} values (using $\lambda_{inc} = 1064$ nm) obtained with the optimally tuned sTD-DFT[DFT] scheme relative to reference TD-DFT (M06-2X/6-311+G(d)) results. Numerical data are reported in Table S1.

that, as detailed in the SI, the error function minimized in the parameterization process includes not only the mean relative absolute error (MRAE) but also the standard deviation between the RAE values of the *trans* and *cis* forms, in order to preserve a reliable $\beta_{\mathrm{HRS}}(trans)/\beta_{\mathrm{HRS}}(cis)$ contrast. Notably, a non zero weight on the standard deviation in the error function was applied for molecules **2**, **3**, **4**, **7** and **8**, for which the optimization led to markedly different RAE values for the two forms.

As shown in Figure 4, except for molecule **4**, sTD-DFT $\beta^{\omega}_{\mathrm{HRS}}$ values deviate by less than 4% from reference values for all compounds in both *trans* and *cis* forms, confirming that sTD-DFT reliably captures β_{HRS} responses across diverse compounds provided optimal, system-dependent, parameters are used. The larger error (7%) obtained for molecule **4** originates from the comparatively smaller β_{HRS} values of this compound (100–800 a.u.) and from the use of a single set of $\{\gamma_J, \gamma_K\}_{opt}$ exponents for the **c1** and **c2** conformers (see Table S1). Relaxing the latest constraint, that is, using distinct sets of parameters for **c1** and **c2**, reduces the error to below 4%, consistent with the other compounds.

As shown in Table S1, the DRs are also qualitatively well reproduced by sTD-DFT, although they are systematically underestimated relative to the reference TD-DFT values for both *trans* and *cis* isomers. Consistent with the trends observed for the β_{HRS} values, the largest deviations occur for molecule **4**.

3.1.2 | Refinement of the sTD-DFT Parameterization for Molecule 10

3.1.2.1 | Increase of the Resolution of the 2D Error Maps. In this section, the sTD-DFT[DFT] parameterization for molecule **10** is refined by increasing the resolution of the error maps, achieved by decreasing the step size of the $\{\gamma_J, \gamma_K\}$ parameters to 0.01. Following the results from Section 3.1.1, the parameter range was limited to 0.05–2.5. The dataset employed in the parameterization procedure is summarized in Table S2. The resulting high-resolution error maps are displayed in Figure 5, from which new optimal parameters, $\{\gamma_J, \gamma_K\}_{opt} = \{0.94, 0.93\}$, are identified. These parameters differ from those obtained in Section 3.1.1 ($\{0.95, 1.15\}$, see Table S1), and yield smaller errors with respect to reference TD-DFT/M06-2X/6-311+G(d) calculations (1.69% and 0.13% for the *trans* and *cis* forms, respectively). These results illustrate the sensitivity of the parameters, in particular γ_K, to the details of the parameterization procedure, as clearly shown by the 2D error maps. They also demonstrate that multiple parameter sets can yield reasonably small errors, depending on the desired level of accuracy.

The same parameterization procedure was repeated with the sTD-DFT[xTB] scheme, using tight-binding MOs for describing the electronic ground-state of the molecule. The optimal parameters, $\{\gamma_J, \gamma_K\}_{opt} = \{1.40, 0.75\}$, yield errors of 0.10% and 0.31% for the *trans* and *cis* forms, respectively.

3.1.2.2 | Parameterization Over a Spectral Range. The sTD-DFT scheme can be parameterized at a specific incident wavelength, as exemplified in the previous sections for $\lambda_{\mathrm{inc}} = 1064$ nm. For broader applicability, the $\{\gamma_J, \gamma_K\}$ parameters can also be tuned to reproduce the full dispersion profile of β^{ω}_{HRS} over a selected spectral range. In this section, this approach is illustrated for molecule **10** over incident wavelengths ranging from 800 to 1800 nm. To this end, a fully automated parameterization procedure has been developed, which involves generating high-resolution 2D error maps analogous to those shown in Figure 5, at every 10 nm intervals. As illustrated in Figure 6, a separate map is produced for each *trans* and *cis* isomers, at each wavelength, resulting in a total of 202 error maps covering the entire spectral range. The MRAE and standard deviations of RAEs are then computed from the 202 error maps and incorporated into the error function to be minimized (see Equation S3). The optimal $\{\gamma_J, \gamma_K\}$ parameters obtained from this procedure are subsequently used to plot the evolution of β^{ω}_{HRS} of the *trans* and *cis* isomers as a function of the incident wavelength in the 600–1800 nm range using steps of 1 nm. This procedure was applied to parameterize both the sTD-DFT[DFT] and sTD-DFT[xTB] schemes. The resulting $\{\gamma_J, \gamma_K\}_{opt}$ values are gathered in Table 1, together with the optimal parameters obtained above for a specific incident wavelength of 1064 nm.

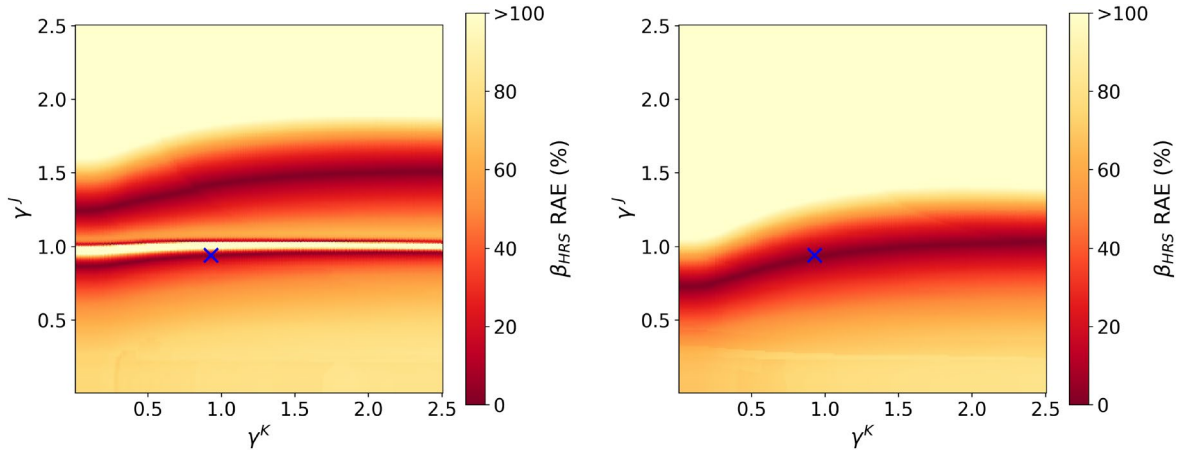

FIGURE 5 | High-resolution 2D error maps of sTDDFT[DFT] on β^{ω}_{HRS} ($\lambda_{\mathrm{inc}} = 1064$ nm) for the *cis* (left) and *trans* (right) forms of molecule **10**, with respect to M06-2X/6-311+G(d) TD-DFT calculations. The new set of optimal parameters ($\{\gamma_J, \gamma_K\}_{\mathrm{opt}} = \{0.94, 0.93\}$), applicable to both *trans* and *cis* forms, is pined with blue crosses.

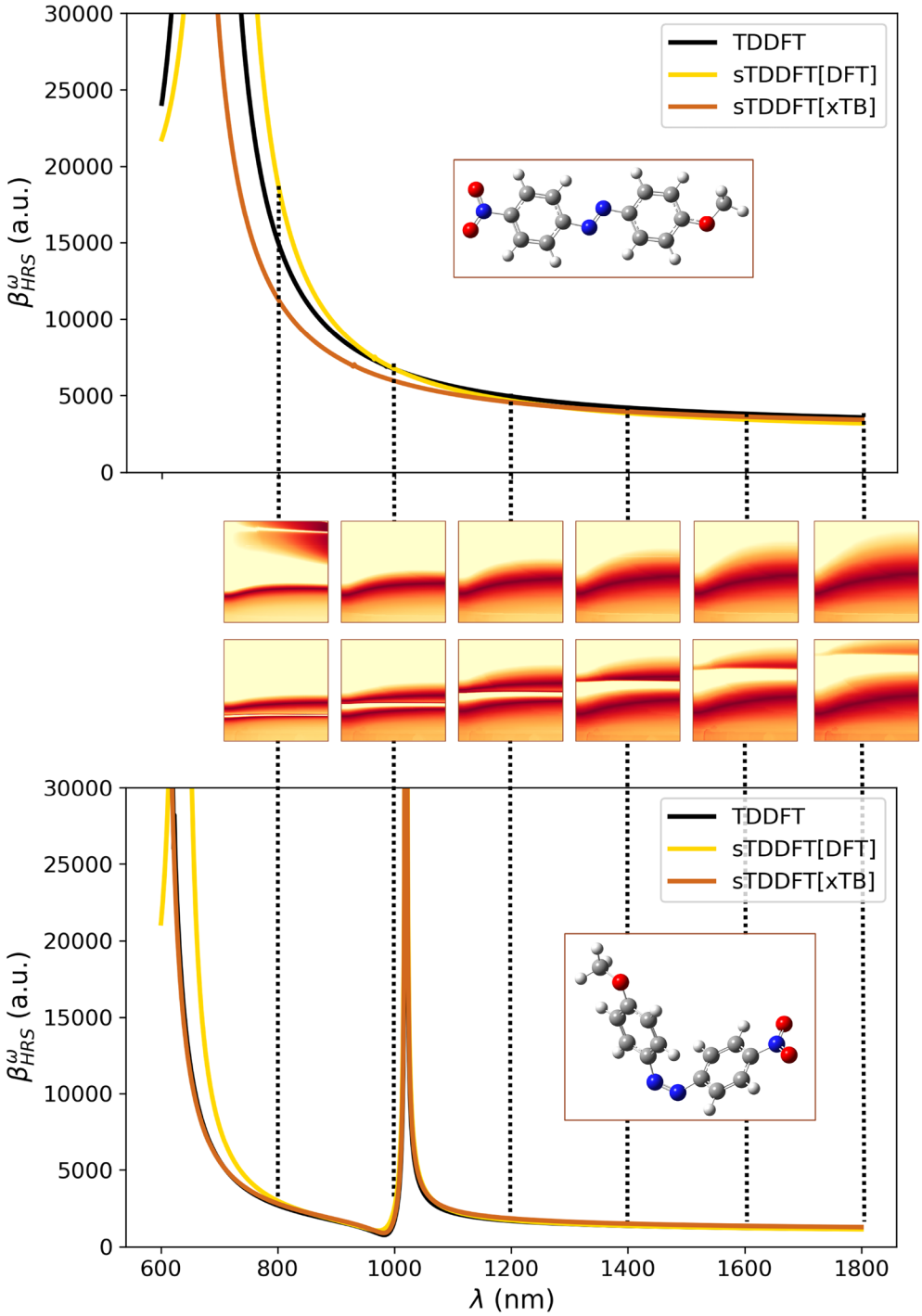

FIGURE 6 | Dispersion profiles of β^{ω}_{HRS}, as calculated for molecule **10** in the *trans* (top) and *cis* (bottom) forms using standard TD-DFT at the M06-2X/6-311G+(d) level, and using the optimally-tuned sTD-DFT[DFT] and sTD-DFT[xTB] schemes. 2D errors maps are generated every 10 nm but displayed only every 200 nm for clarity. An outlier point at 929 nm has been removed from the sTDDFT[xTB] curve.

As shown in Figure 6, the sTD-DFT[DFT] method using optimally-tuned parameters accurately reproduces the dispersion profiles for both isomers. Remarkably, although near-resonant wavelengths in the 600–790 nm region were excluded from the parameterization process (in order to avoid large RAE values in the parameterization), the resulting optimal parameters still capture the enhancement of the NLO response associated with frequency resonance in this spectral range. Moreover, the sTD-DFT[xTB] scheme is also found to well reproduce the influence of frequency dispersion on β^{ω}_{HRS}, especially for the *cis* form.

Another important observation is that, independently of whether DFT or xTB is used to generate the ground-state MOs, the sTD-DFT$_{1064}$ and sTD-DFT$_{800\text{-}1800}$ parameterizations mainly differ in the value of the γ_K parameter, whereas the γ_J parameter remains relatively similar in both cases. This can be rationalized by the fact that γ_K has a strong influence on the position of the optical resonances, as illustrated in Figure S4 for sTD-DFT[xTB] calculations. Consequently, the parameterizations over the 800–1800 nm spectral window primarily translate into adjustments of γ_K.

TABLE 1 | Dynamic ($\lambda_{inc} = 1064$ nm) β_{HRS} values calculated on equilibrium geometries for the *trans* and *cis* forms of molecule **10** using the sTD-DFT[DFT] and sTD-DFT[xTB] schemes with $\{\gamma_J, \gamma_K\}_{opt}$ parameters optimized for a 1064 nm wavelength and for the full 800–1800 spectral range.

Method	Form	$\{\gamma_J, \gamma_K\}_{opt}$	β_{HRS}	$\eta_{\beta_{HRS}}$
TD-DFT	*trans*	—	5917	2.07
	cis		2859	
sTD-DFT[DFT]$_{1064}$	*trans*	{0.94, 0.93}	6017	2.10
	cis		2862	
sTD-DFT[xTB]$_{1064}$	*trans*	{1.64, 0.75}	5923	2.08
	cis		2850	
sTD-DFT[DFT]$_{800\text{-}1800}$	*trans*	{0.96, 1.26}	5783	1.85
	cis		3118	
sTD-DFT[xTB]$_{800\text{-}1800}$	*trans*	{1.73, 1.22}	5337	1.72
	cis		3095	

Considering the β_{HRS} values at $\lambda_{inc} = 1064$ nm, the results obtained using sTD-DFT with parameters optimized over the 800–1800 nm range yield, as expected, larger RAEs (2.3% and 9.1% for *trans* and *cis*, respectively, at the sTD-DFT[DFT] level, and 9.8% and –8.3% at the sTD-DFT[xTB] level) compared to the value computed with the $\{\gamma_J, \gamma_K\}$ parameters optimized at this specific wavelength (see Table 1). Yet, these errors remain acceptably small. The *trans*/*cis* β_{HRS} contrast ($\eta_{\beta_{HRS}}$) is also well reproduced, although slightly underestimated. Moreover, it is noteworthy that both xTB- and DFT-based sTD-DFT implementations perform equally well, suggesting that the specific choice of ground-state MOs becomes secondary once the parameterization is applied.

3.1.3 | Impact of Geometrical Distortions of Individual Molecular Fragments

In the previous sections, the molecules were treated in their equilibrium geometries. However, the AZO units within a SAM adopt highly distorted, non-equilibrium structures due to surface confinement and steric constraints. To be applicable to highly disordered materials, the sTD-DFT method must therefore account for the influence of these distortions on the targeted properties. In this section, we evaluate the ability of the optimally tuned sTD-DFT[DFT] and sTD-DFT[xTB] schemes—using $\{\gamma_J, \gamma_K\}_{opt}$ parameters determined for molecule **10** (Table 1)—to reproduce the NLO responses of individual molecular fragments extracted from MD simulations of AZO-based SAMs. A total of 610 monomer geometries are considered for each configuration, namely the *trans* and *cis* forms. Note that the molecular fragments considered in this section differ from molecule **10**, as they include both the photoswitchable AZO unit and the alkyl linker, as schematized in Figure 1c.

The distributions of the dynamic ($\lambda_{inc} = 1064$ nm) HRS hyperpolarizability (β_{HRS}), together with those of the β vector norm, the normal component β_z, and the nonlinear anisotropy parameter a_β (Equations (4–6)), computed at the sTD-DFT[DFT] and sTD-DFT[xTB] levels, are shown in Figure 7 for *trans* SAMs, together with the corresponding reference TD-DFT/M06-2X/6-311+G(d) distributions. The associated average values and standard deviations are summarized in Table 2. Results obtained for *cis* SAMs, as well as for static NLO responses, are provided in Figures S5–S7 and Table S4.

These results demonstrate that the sTD-DFT method successfully reproduces both the average values and the dispersion of the NLO responses for the two isomers, regardless of the parameter set employed (1064 nm or 800–1800 nm) or the choice of ground-state MOs (DFT- or xTB-derived). As expected, the sTD-DFT[DFT] scheme with parameters optimized at $\lambda = 1064$ nm shows the best agreement with the reference TD-DFT hyperpolarizability values for both the *trans* and *cis* configurations of the SAM. The average values of β and β_z, as well as the NLO contrasts upon photoisomerization, are quantitatively reproduced. The slightly larger anisotropy factor of the *cis* SAM is also captured, except at the sTD-DFT[DFT]$_{1064}$ level. Using the $\{\gamma_J, \gamma_K\}$ parameters optimized over the broader 800–1800 nm range leads to distributions that are more shifted relative to the reference TD-DFT calculations, resulting in slightly underestimated β and overestimated β_z contrasts. Finally, although the overall trends remain in qualitative agreement with the TD-DFT reference, employing xTB instead of DFT to generate the ground-state MOs yields somewhat less quantitative results, likely due to the much smaller basis set, which is less sensitive to subtle geometrical variations.

3.1.4 | Impact of Intermolecular Interactions in Model Dimers

In addition to geometrical distortions of the molecular fragments, aggregation effects such as electronic polarization and intermolecular couplings may play a crucial role in densely packed SAMs. In this section, we evaluate the ability of the sTD-DFT scheme to describe these effects and their impact on the NLO responses, using a model system consisting of two AZO molecules in their *trans* equilibrium geometry. The initial dimer is constructed by duplicating the optimized geometry of molecule **10** and placing the two units at a standard π-stacking distance of 3.50 Å (Figure 8). To probe a range of packing configurations, one molecule is systematically translated or rotated relative to the other. Translations are performed along the molecular long (x) and short (y) axes, varying x and y within the ranges $[-5; +5]$ Å by steps of 0.2 Å, while rotations are explored by varying the relative angle θ between $-90°$ and $+90°$ by steps of 1°. This sampling enables mapping of how structural variations modulate the NLO properties. The impact of intermolecular interactions is quantified using the κ ratio, as defined in Equation (23).

$$\kappa = \frac{\beta_{HRS}(dimer)}{2\beta_{HRS}(monomer)}. \tag{23}$$

A value of $\kappa = 1$ indicates that the β_{HRS} response of the dimer is simply the sum of the individual monomer contributions, meaning that intermolecular interactions have negligible impact.

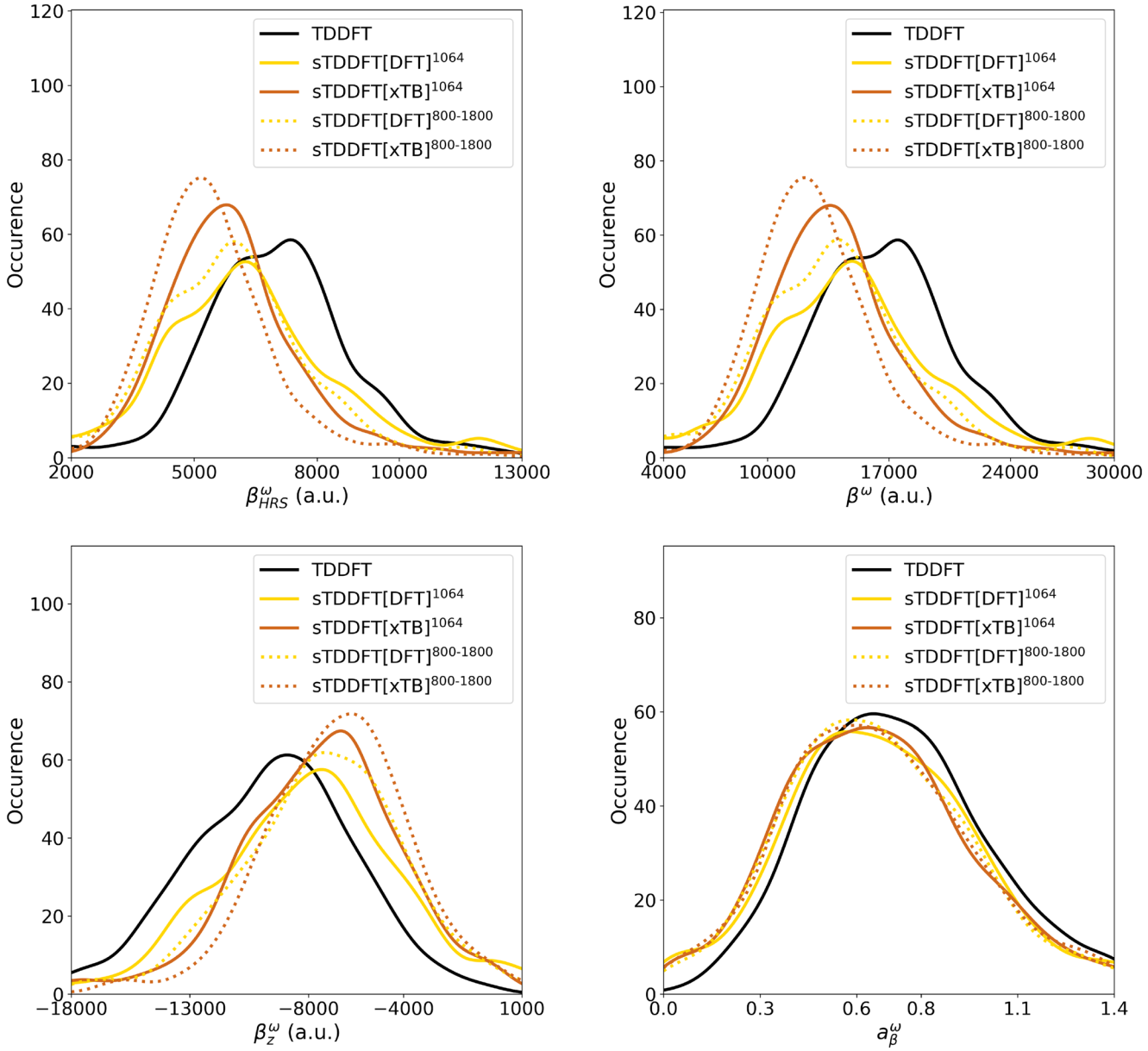

FIGURE 7 | Statistical distributions of the dynamic NLO responses β_{HRS}, β, β_z and a_β calculated on individual molecular residues extracted from MD simulations of AZO-based SAMs in their *trans* configuration. Each distribution was constructed using a non-normalized Gaussian kernel density estimator (KDE), as detailed in Section S4.1.

Conversely, $\kappa < 1$ ($\kappa > 1$) reflects a reduction (enhancement) of the HRS signal due to aggregation effects.

We first examined one-dimensional translations along the x and y axes (see Figure 9a and b for the dynamic results and Figures S8a and S8b for the static ones). The evolution of the κ ratio predicted by sTD-DFT qualitatively reproduces the reference TD-DFT profile, with $\kappa < 1$ for all translations and a minimum at the fully superimposed configuration $(x, y) = (0, 0)$. This behavior is consistent with simple electrostatic considerations: when two molecules are stacked face-to-face, the dipole induced in one unit generates a counteracting field that reduces the effective field experienced by the other, thus lowering the β response [58]. Quantitatively, all sTD-DFT variants tend to overestimate the κ values relative to TD-DFT, indicating that aggregation-induced depolarization effects are underestimated, which is not surprising given that the parameterization was performed for a single isolated molecule. The sTD-DFT[DFT] approach performs slightly better than sTD-DFT[xTB], and the $\{\gamma_J, \gamma_K\}$ parameters optimized over the broader 800–1800 nm range yield marginally improved agreement compared to those optimized at 1064 nm, likely due to error compensation.

The evolution of the κ ratio upon molecular rotation is shown in Figure 9c and Figure S8c. The reference TD-DFT profile exhibits a minimum at $\theta = 0°$ and local maxima around $\theta = \pm 60°$. This behavior is qualitatively reproduced by the sTD-DFT calculations, although the predicted maxima occur at lower rotation angles, regardless of the parameter set or ground-state MOs employed. As observed for translations, the 800–1800 nm

TABLE 2 | Average values and standard deviations of the dynamic NLO responses β_{HRS}, β, β_z (in a.u.) and a_β calculated on individual molecular residues extracted from the *trans* and *cis* SAMs. The NLO contrasts $\eta_\beta = \beta(trans)/\beta(cis)$ and $\eta_{\beta_z} = \beta_z(trans)/\beta_z(cis)$ are also reported.

Method	SAM	β_{HRS}	β	β_z	a_β	η_β	η_{β_z}
TD-DFT	*trans*	7052±1916	16,771±4614	−9595±4134	0.751±0.307	—	—
	cis	3057±6240	7017±14250	−2146±5491	0.929±0.958	2.39	4.47
sTD-DFT[DFT]$_{1064}$	*trans*	6962±5260	16,525±12,530	−8130±8245	0.706±0.337	—	—
	cis	3346±4598	6950±9259	−1871±5302	0.704±0.688	2.38	4.35
sTD-DFT[xTB]$_{1064}$	*trans*	6039±2073	14,252±4827	−7534±3748	0.683±0.323	—	—
	cis	4265±10,794	9437±23,727	−1493±17,065	1.125±1.130	1.51	5.05
sTD-DFT[DFT]$_{800\text{-}1800}$	*trans*	6551±5350	15,391±12,591	−7301±9044	0.698±0.340	—	—
	cis	3566±8588	7217±15,577	−1528±5192	0.745±0.849	2.13	4.78
sTD-DFT[xTB]$_{800\text{-}1800}$	*trans*	5576±2413	13,156±5702	−6704±5925	0.688±0.330	—	—
	cis	2839±3740	6314±7622	−2030±6309	1.173±1.197	2.08	3.30

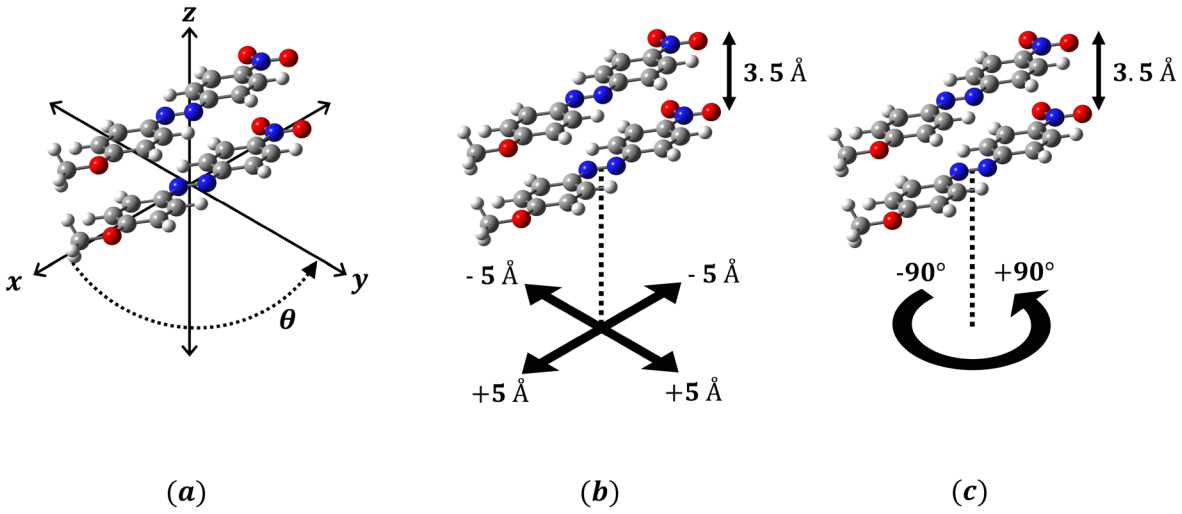

FIGURE 8 | Coordinate system (a), translation (b) and rotation (c) schemes of the model dimer.

parameterization yields κ values slightly closer to the reference data than the 1064 nm parameterization, and using DFT-derived MOs provides better agreement than using xTB-derived MOs.

Finally, we extended our analysis to a full two-dimensional mapping, considering simultaneous translations along both the short and long molecular axes, and generated 2D error maps reporting the RAEs of the κ ratio computed with sTD-DFT relative to the reference TD-DFT results (Figures S9 and S10). The results indicate that the sTD-DFT[DFT]$_{800\text{-}1800}$ scheme yields κ values with RAEs ranging from 5.9% to 23.3%, whereas sTD-DFT[DFT]$_{1064}$ yields RAEs between 7.3% and 31.1%.

3.1.5 | Impact of Intermolecular Interactions in Increasingly Large AZO Clusters

The final validation step of the optimally-tuned sTD-DFT approach involves calculating the NLO responses of increasingly large supramolecular aggregates obtained from MD simulations, thereby accounting for both geometrical distortions and intermolecular interactions. In practice, a set of 10 uncorrelated structural frames (each containing 61 AZO units and 60 non functionalized dodecylsilyl chains, see Figure 1b) was extracted from the MD runs of both *trans* and *cis* SAMs, from which disk-shaped clusters were generated by expanding a radius R around the central molecule, and incorporating all fragments whose center of mass falls within that radius (Figure 10). The dynamic β value of each cluster, normalized by the number of photochromic units (N^{AZO}), was then calculated, and the resulting β/N^{AZO} values for clusters with identical radii were averaged, ensuring both temporal and spatial geometrical sampling. Note that two clusters with identical radii R may contain a different number of molecules, depending on the MD frame from which they were extracted.

Owing to the large size of the systems, the $\{\gamma_J, \gamma_K\}$ parameters were first optimized for the *trans* molecule based on TD-DFT/M06-2X calculations using the reduced 6-31G(d) basis set (leading to $\{\gamma_J, \gamma_K\}^{1064}_{\text{opt}} = \{1.65, 1.37\}$), while xTB ground-state MOs were employed for the subsequent sTD-DFT calculations.

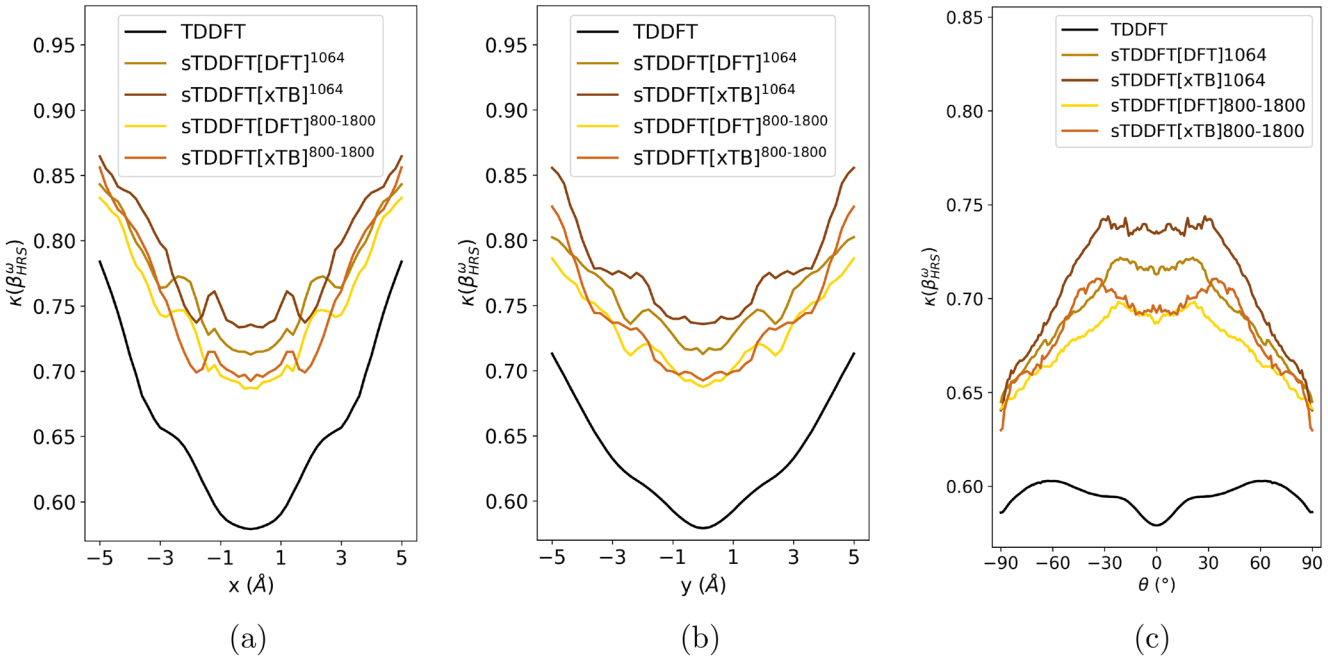

FIGURE 9 | κ ratio of dynamic β_{HRS} values (Equation (23)), calculated for translations along the x (a) and y (b) molecular axes, and for rotations (c). See Figure S8 for the corresponding static results.

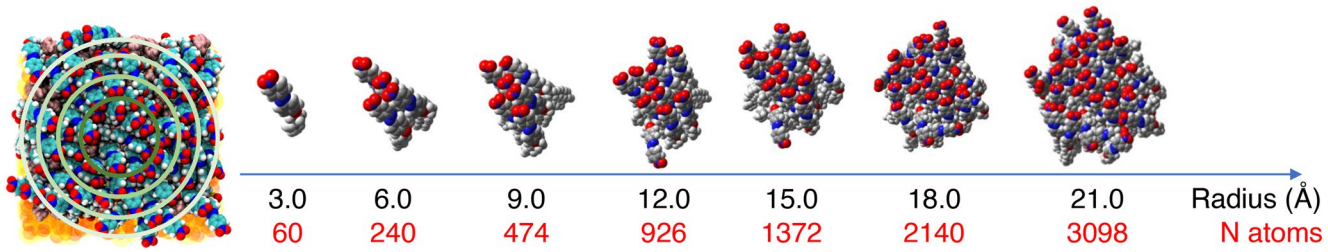

FIGURE 10 | Example of increasing-size supramolecular clusters considered for the NLO calculations, with their radius and the total number of atoms.

The evolution of the dynamic ($\lambda_{inc} = 1064$ nm) NLO responses ($\langle \beta_{HRS}/N^{AZO} \rangle, \langle \beta/N^{AZO} \rangle, \langle \beta_z/N^{AZO} \rangle$, and $\langle a_\beta \rangle$) as a function of the cluster size, computed at the sTD-DFT[xTB] level, is compared in Figure 11 to the reference TD-DFT/M06-2X/6-31G(d) results. Note that, due to numerical instabilities in the TD-DFT calculations for some clusters, one structural frame was excluded, so that each data point in Figure 11 corresponds to the average of nine calculations performed on distinct clusters.

These preliminary results evidence that the sTD-DFT predictions are in excellent agreement with the reference TD-DFT calculations. Therefore, although results in Section 3.1.4 demonstrated that the use of parameters optimized on a single molecule may lead to an underestimation of aggregation effects in highly overlapping model dimers, the sTD-DFT approach appears to be sufficiently reliable for treating large, more realistic supramolecular systems. The evolution of $\langle \beta_{HRS}/N^{AZO} \rangle$ and $\langle \beta/N^{AZO} \rangle$ with the cluster size shows a progressive decrease of the first hyperpolarizability, while the normal β_z component progressively increases and saturates for large clusters ($R > 10$ Å). The nonlinear anisotropy oscillates between 0.67 and 0.98, which indicates that the in-plane components dominate over the normal ones, independently of the cluster size. Note that the abrupt increase in $\langle \beta_{HRS}/N^{AZO} \rangle, \langle \beta/N^{AZO} \rangle$ and $\langle \beta_z/N^{AZO} \rangle$ observed for $R = 21$ Å arises from frequency-dispersion effects: Within these clusters, some molecules exhibit distorted geometries that place an excited state close to resonance with the second-harmonic wavelength (532 nm). This interpretation is supported by the evolution of the static NLO responses (Figure S11), for which this abrupt increase is no longer observed.

In a second step, similar calculations were carried out for both *trans* and *cis* SAMs using the sTD-DFT[xTB] and sTD-DFT[DFT] schemes, with the $\{\gamma_J, \gamma_K\}_{opt}$ parameters listed in Table 1. sTD-DFT[DFT] calculations were performed based on M06-2X/6-311+G(d) ground-state MOs. The evolution with cluster size of the dynamic NLO responses of *trans* SAMs are reported in Figure 12, and compared to reference TD-DFT/M06-2X/6-311+G(d) calculations. Results obtained for static properties are reported in Figure S15, as well as the evolution with cluster size of the dynamic $\langle \beta_{HRS}/N^{AZO} \rangle$ values calculated for each individual MD frame (Figures S12 and S13).

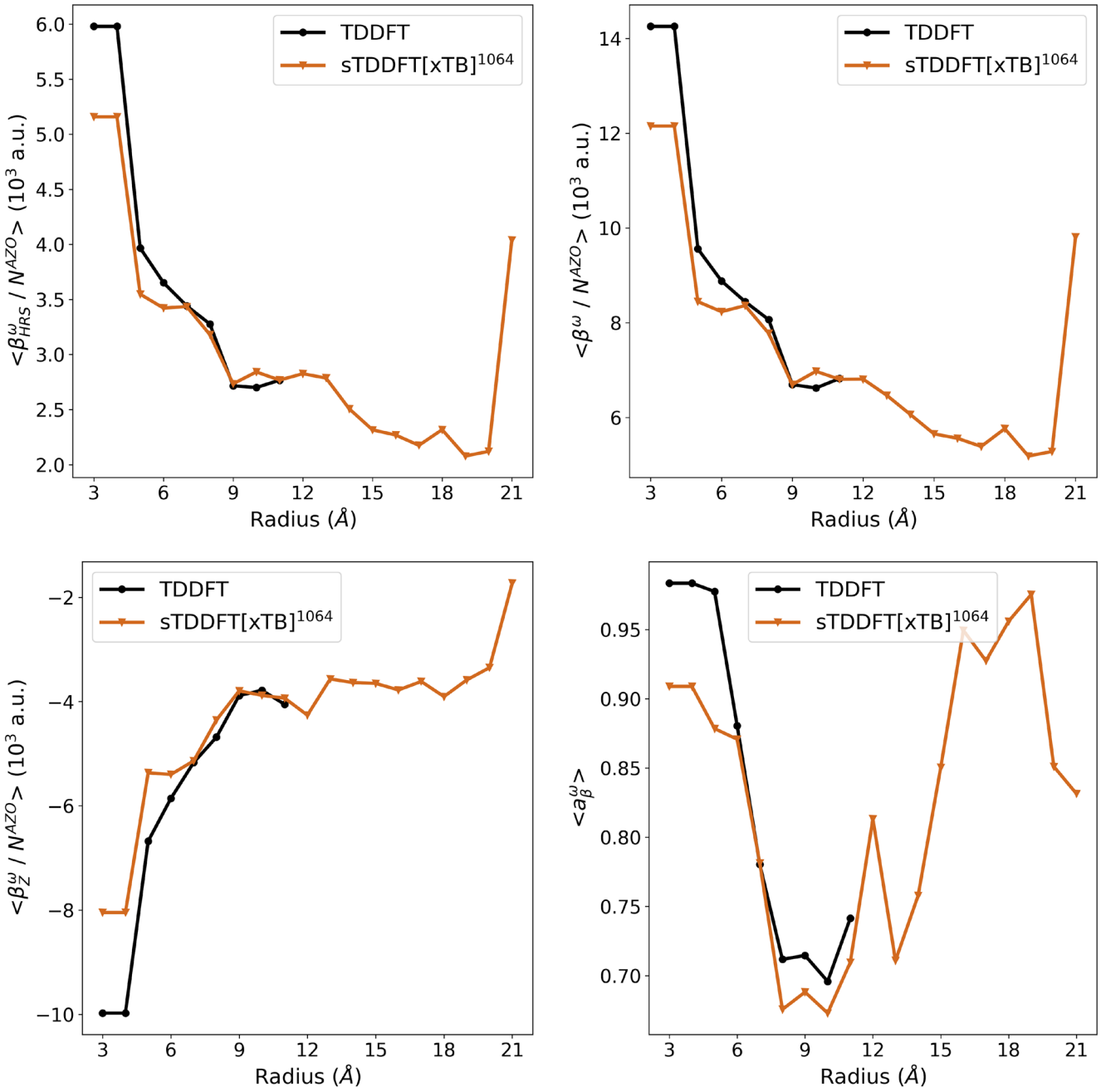

FIGURE 11 | Evolution with cluster size of the dynamic NLO responses $\langle \beta_{HRS}/N^{AZO} \rangle$, $\langle \beta/N^{AZO} \rangle$, $\langle \beta_z/N^{AZO} \rangle$, and $\langle a_\beta \rangle$, calculated for *trans* clusters at the TD-DFT/M06-2X/6-31G(d) level and using the optimally-tuned sTD-DFT[xTB] scheme with $\{\gamma_J, \gamma_K\}^{1064}_{\text{opt}} = \{1.65, 1.37\}$. Each data point corresponds to the average of nine calculations performed on distinct clusters.

With the 6-311+G(d) basis set, standard TD-DFT calculations are only tractable for clusters with radius smaller than 9 Å. The NLO responses follow the same trend as reported in Figure 11, showing a progressive decrease in $\langle \beta_{HRS}/N^{AZO} \rangle$ and $\langle \beta/N^{AZO} \rangle$ with increasing cluster size, together with a concurrent increase and subsequent saturation of $\langle \beta_z/N^{AZO} \rangle$. The NLO responses computed for the *cis* clusters, shown in Figures S14 and S16 for dynamic and static responses, respectively, exhibit a much less monotonic evolution with increasing cluster size. Again, these irregular trends can be attributed to the highly distorted geometries adopted by certain molecular fragments within the *cis* SAM, which lead to frequency resonances at the second harmonic. In addition, as previously reported in Reference [5], residual *trans* fragments remain in the *cis* SAM due to the incomplete photoisomerization yield (95%) obtained after convergence of the MD simulations. As the cluster size increases, the inclusion of such *trans* units further contributes to the non monotonic behavior of the NLO responses.

Overall, these calculations on progressively larger clusters demonstrate that the optimally tuned sTD-DFT approach provides a robust framework for assessing the NLO responses of large supramolecular aggregates, enabling the treatment of all aggregation effects at a full QM level.

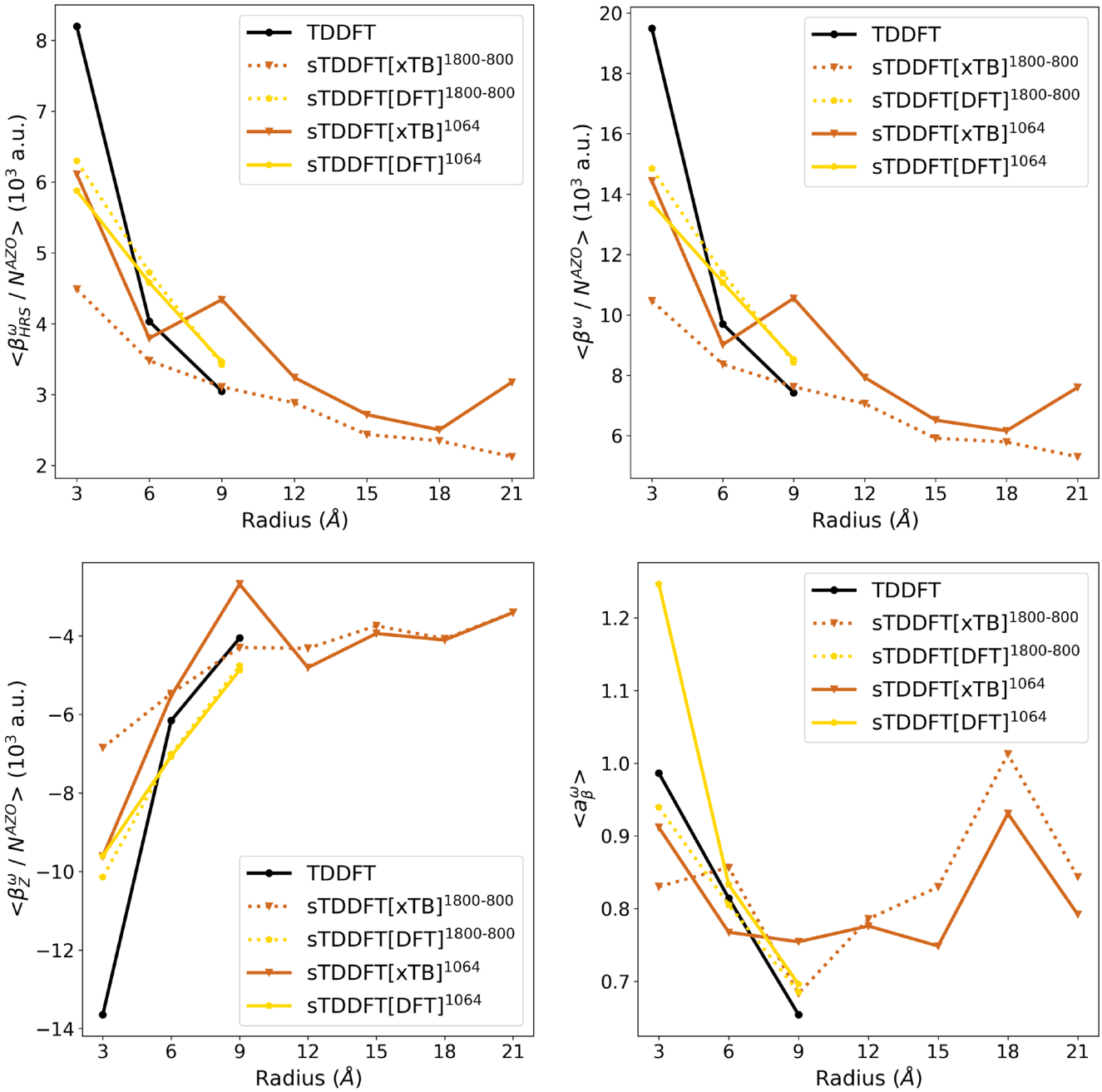

FIGURE 12 | Evolution with cluster size of the dynamic NLO responses $\langle \beta_{HRS}/N^{AZO} \rangle$, $\langle \beta/N^{AZO} \rangle$, $\langle \beta_z/N^{AZO} \rangle$, and $\langle a_\beta \rangle$, calculated for *trans* clusters at the TD-DFT/M06-2X/6-311+G(d) level and using the optimally-tuned sTD-DFT [DFT] and sTD-DFT [xTB] schemes (the $\{\gamma_J, \gamma_K\}_{opt}$ parameters are listed in Table 1). Each data point corresponds to the average of nine calculations performed on distinct clusters.

3.2 | SHG Responses of AZO Monolayers

In this final section, we discuss further the results obtained on the largest clusters with radius $R = 21$ Å (i.e., containing between 27 and 32 photoswitchable molecular units and an equivalent number of non functionalized alkyl chains). The NLO responses (averaged over 10 frames) computed at the sTD-DFT[xTB]$_{1064}$ level are gathered in Table 3 for both *trans* and *cis* SAMs, in comparison to those determined for the isolated fragments (averaged over 610 monomers, Table 2), while neglecting aggregation effects. Static results taken from our previous work [5], in which intermolecular interactions were modeled at the TD-DFT/M06-2X/6-311+G(d) level using an electrostatic embedding composed of point charges (PCs) located at the atomic positions of neighboring chromophores, referred to as TD-DFT[PC], are also reported in Table 3 for comparison.

Accounting for intermolecular interactions at the QM level using sTD-DFT leads to a pronounced decrease of the static β and β_z values for both the *trans* and *cis* SAMs, as highlighted by the κ_β and κ_{β_z} ratios (Table 3). This finding is consistent with

TABLE 3 | Average values of the dynamic NLO responses β_{HRS}, β, β_z (in a.u.) and a_β calculated at the sTD-DFT[xTB]$_{1064}$ level for isolated molecular fragments and for the largest molecular clusters (with radius $R = 21$Å) extracted from the *trans* and *cis* SAMs. The NLO contrasts $\eta_\beta = \beta(trans)/\beta(cis)$ and $\eta_{\beta_z} = \beta_z(trans)/\beta_z(cis)$ ratios, as well as the $\kappa_\beta = \beta(\text{clusters})/\beta(\text{fragments})$ and $\kappa_{\beta_z} = \beta_z(\text{clusters})/\beta_z(\text{fragments})$ ratios, are reported in the last columns. TD-DFT[PC] results, from Reference [5], are reported for comparison.

System	SAM	β_{HRS}	β	β_z	a_β	η_β	η_{β_z}	κ_β	κ_{β_z}
Static TD-DFT results from Reference [5]									
Isolated fragments	*trans*	—	8497	−8028	0.76	—	—	—	—
	cis	—	2904	−2805	0.90	2.86	3.38	—	—
Fragments + PC	*trans*	—	4582	−2230	0.66	—	—	0.54	0.28
	cis	—	2480	−767	0.71	1.85	2.91	0.85	0.27
Static sTD-DFT[xTB]$_{1064}$ results									
Isolated fragments	*trans*	3143	7382	−3908	0.67	—	—	—	—
	cis	1221	2949	−1537	1.08	2.51	2.54	—	—
Clusters	*trans*	1488	3777	−2495	0.88	—	—	0.51	0.64
	cis	467	1211	−1188	5.73	3.12	2.10	0.41	0.77
Dynamic sTD-DFT[xTB]$_{1064}$ results									
Isolated fragments	*trans*	6962	14,252	−7534	0.68	—	—	—	—
	cis	4265	9437	−1493	1.13	1.51	5.05	—	—
Clusters	*trans*[a]	3177	7593	−3407	0.79	—	—	0.53	0.45
	cis	2559	5969	−3758	7.02	1.27	0.91	0.43	2.52

[a]One frame was excluded from the calculation of the average values.

TD-DFT[PC] results, which confirms that using a PC embedding is a reliable approximation for qualitatively capturing intermolecular interaction effects on the NLO responses in these supramolecular aggregates. Also consistent with TD-DFT[PC] results, the anisotropy ratio for the *trans* SAM is smaller than unity, indicating that the in-plane contributions dominate over the normal β_z component. This ratio slightly increases from 0.67 to 0.88 when aggregation effects are explicitly accounted for, whereas a small decrease (from 0.76 to 0.66) is predicted using the TD-DFT[PC] model. This trend is even more pronounced for the *cis* SAMs, for which a_β calculated with sTD-DFT increases dramatically from 1.08 to 5.73 when going from isolated fragments to supramolecular clusters, while a decrease from 0.90 to 0.71 is observed with TD-DFT[PC]. Besides, both TD-DFT[PC] and sTD-DFT calculations predict *trans*/*cis* β contrasts (η_β) of the same order of magnitude. However, while considering only the electrostatic environment leads to a reduction of this contrast, including intermolecular interactions at the full QM level results in an increase. Conversely, TD-DFT[PC] calculations predict a comparable decrease in η_{β_z} (from 3.38 to 2.91), in line with the trend obtained using sTD-DFT.

Comparison between static and dynamic sTD-DFT results reveals that resonance effects enhance the NLO responses of both *trans* and *cis* clusters. However, this enhancement is significantly stronger for the *cis* SAMs, resulting in smaller dynamic η_β contrasts compared to the static values. The anisotropy factors obtained from static and dynamic calculations are nearly identical, indicating that frequency dispersion has little influence on the symmetry of the NLO responses. Likewise, the static and dynamic κ_β ratios for both *trans* and *cis* SAMs are very similar, suggesting that aggregation and frequency dispersion effects are independent from each other. In contrast, the κ_{β_z} ratio for the *cis* SAM shows a marked difference between static and dynamic values, due to the strong enhancement of the dynamic β_z component under resonance conditions.

4 | Conclusion

This study presents a fully automated protocol for the optimization and validation of the exponents of the two-electron integrals in the sTD-DFT framework, enabling the reproduction of NLO responses obtained with conventional TD-DFT at a fraction of the computational cost. The sTD-DFT approach is employed using ground-state MOs generated either from DFT calculations or, for further computational savings, from xTB calculations. For practical usability, the parameterization is deliberately kept simple and performed on isolated molecules in their equilibrium geometry. Statistical samplings of out-of-equilibrium molecular geometries, along with increasingly large supramolecular aggregates extracted from previously reported MD simulations of AZO SAMs, are subsequently employed as a testing ground to evaluate the transferability of the optimally tuned parameters. The results show that sTD-DFT[xTB] yields NLO responses in close agreement with those obtained from standard TD-DFT calculations, and enables the prediction of the NLO properties of large aggregates that lie beyond the practical computational

limits of conventional TD-DFT. This study therefore demonstrates that combining MD simulations with optimally tuned sTD-DFT provides a powerful and practical strategy for evaluating the NLO responses of large supramolecular aggregates with highly disordered morphologies, while fully capturing aggregation effects at a full quantum-mechanical level.

Comparison of the NLO responses computed for supramolecular clusters with those obtained from statistical ensembles of individual fragments, both extracted from MD trajectories, enables a quantitative evaluation of aggregation effects, which are found to induce a significant decrease in the second-harmonic signal. Furthermore, comparison with previously reported results, in which intermolecular interactions were modeled using a point-charge embedding, shows that this simple electrostatic approach remains suitable for qualitatively describing the influence of intermolecular interactions on the NLO responses of supramolecular aggregates. However, the *trans*/*cis* NLO contrasts and the anisotropy of the NLO signal can differ significantly when aggregation effects are treated at the QM level, indicating that reliable quantitative estimates require an explicit QM description of intermolecular interactions.

Improvements to the parameterization process can be envisaged. In particular, the optimal tuning of the two-electron integral parameters could be performed using small model clusters rather than isolated molecules, allowing a more accurate reproduction of aggregation effects on the targeted NLO properties. However, this would come at the expense of the simplicity that makes the interest of this semi-empirical scheme. Similarly, instead of considering the global NLO response of the molecule such as the HRS first hyperpolarizability, parameterization could be based on specific components of the β tensor, potentially providing a better description of the anisotropy of the NLO responses. Yet, again, this would induce a loss in term of methodological simplicity.

A more promising direction for future work is the coupling of the sTD-DFT scheme with linear-scaling (LS) DFT methods, which exploit the localized nature of the density matrix and allow the computational workload to scale linearly with the size of the system [59]. LS-DFT is expected to provide more accurate ground-state MOs than xTB, potentially improving the reliability of the resulting NLO predictions. Alternatively, one can adopt a strategy that avoids the tailored parameterizations and benchmarks required by the sTD-DFT approach. The very recent development of the eXact integral sTD-DFT method (XsTD-DFT) by de Wergifosse and coworkers offers a promising solution, eliminating the empirical aspects of sTD-DFT approaches based on MNOK 2-electron integrals, and ensuring greater transferability across systems [60–62]. These computational approaches are currently being tested in our laboratories.

Acknowledgments

M.G.M. thanks the F.R.S.-FNRS for her Research Fellow position. This work received financial support from the French National Research Agency (Grant number ANR-20-CE29-0009-01), the Idex Bordeaux (Research Program GPR Light) and the EUR Light S&T (PIA3 Program, ANR-17-EURE-0027). Calculations were performed using the computing facilities provided by the Mésocentre de Calcul Intensif Aquitain (MCIA) of the Université de Bordeaux and the Université de Pau et des Pays de l'Adour.

Funding

This work was supported by the Agence Nationale de la Recherche (Grant No. ANR-20-CE29-0009-01).

Data Availability Statement

All molecular structures and properties of isolated molecules, model dimers, MD-generated residues, and aggregates are provided as Supporting Information in a ZIP archive. Detailed instructions for accessing the data are provided in a README file.

References

1. M. Schulze, M. Utecht, A. Hebert, K. Rück-Braun, P. Saalfrank, and P. Tegeder, "Reversible Photoswitching of the Interfacial Nonlinear Optical Response," *Journal of Physical Chemistry Letters* 6 (2015): 505–509.

2. M. Schulze, M. Utecht, T. Moldt, et al., "Nonlinear Optical Response of Photochromic Azobenzene-Functionalized Self-Assembled Monolayers," *Physical Chemistry Chemical Physics* 17 (2015): 18079–18086.

3. C. Tonnelé, K. Pielak, J. Deviers, L. Muccioli, B. Champagne, and F. Castet, "Nonlinear Optical Responses of Self-Assembled Monolayers Functionalized With Indolino-Oxazolidine Photoswitches," *Physical Chemistry Chemical Physics* 20 (2018): 21590–21597.

4. C. Tonnelé, B. Champagne, L. Muccioli, and F. Castet, "Nonlinear Optical Contrast in Azobenzene-Based Self-Assembled Monolayers," *Chemistry of Materials* 31 (2019): 6759–6769.

5. A. Dellai, L. Muccioli, F. Castet, and C. Tonnelé, "Second Harmonic Response of Azobenzene Self-Assembled Monolayers: The Effect of Push/Pull Substitution," *Journal of Physical Chemistry C Nanomaterials and Interfaces* 129 (2025): 8417–8428.

6. F. Castet, C. Tonnelé, L. Muccioli, and B. Champagne, "Predicting the Second-Order Nonlinear Optical Responses of Organic Materials: The Role of Dynamics," *Accounts of Chemical Research* 55 (2022): 3716–3726.

7. K. J. de Almeida, K. Coutinho, W. B. de Almeida, W. R. Rocha, and S. Canuto, "A Monte Carlo–Quantum Mechanical Study of the Solvatochromism of Pyrimidine in Water and in Carbon Tetrachloride," *Physical Chemistry Chemical Physics (PCCP)* 3 (2001): 1583–1587.

8. K. Coutinho and S. Canuto, "The Sequential Monte Carlo-Quantum Mechanics Methodology. Application to the Solvent Effects in the Stokes Shift of Acetone in Water," *Journal of Molecular Structure, Theochem* 632 (2003): 235–246.

9. K. Coutinho, R. Rivelino, H. C. Georg, and S. Canuto, *The Sequential QM/MM Method and its Applications to Solvent Effects in Electronic and Structural Properties of Solutes*, (Springer, 2008).

10. N. De Mitri, S. Monti, G. Prampolini, and V. Barone, "Absorption and Emission Spectra of a Flexible Dye in Solution: A Computational Time-Dependent Approach," *Journal of Chemical Theory and Computation* 9 (2013): 4507–4516.

11. W. Arbelo-González, R. Crespo-Otero, and M. Barbatti, "Steady and Time-Resolved Photoelectron Spectra Based on Nuclear Ensembles," *Journal of Chemical Theory and Computation* 12 (2016): 5037–5049.

12. F. Kossoski and M. Barbatti, "Nuclear Ensemble Approach With Importance Sampling," *Journal of Chemical Theory and Computation* 14 (2018): 3173–3183.

13. J. Cerezo, J. Gierschner, F. Santoro, and G. Prampolini, "Explicit Modelling of Spectral Bandshapes by a Mixed Quantum-Classical Approach: Solvent Order and Temperature Effects in the Optical Spectra of Distyrylbenzene," *ChemPhysChem* 25 (2024): e202400307.

14. K. Pielak, C. Tonnelé, L. Sanguinet, et al., "Dynamical Behavior and Second Harmonic Generation Responses in Acido-Triggered Molecular Switches," *Journal of Physical Chemistry C Nanomaterials and Interfaces* 122 (2018): 26160–26168.

15. T. N. Ramos, S. Canuto, and B. Champagne, "Unraveling the Electric Field-Induced Second Harmonic Generation Responses of Stilbazolium Ion Pairs Complexes in Solution Using a Multiscale Simulation Method," *Journal of Chemical Information and Modeling* 60 (2020): 4817–4826.

16. C. Naim, R. Vangheluwe, I. Ledoux-Rak, et al., "Electric-Field Induced Second Harmonic Generation Responses of Push–Pull Polyenic Dyes: Experimental and Theoretical Characterizations," *Physical Chemistry Chemical Physics* 25 (2023): 13978–13988.

17. A. Dellai, C. Naim, J. Cerezo, G. Prampolini, and F. Castet, "Dynamic Effects on the Nonlinear Optical Properties of Donor Acceptor Stenhouse Adducts: Insights From Combined MD+QM Simulations," *Physical Chemistry Chemical Physics* 26 (2024): 13639–13654.

18. A. Dellai, C. Naim, T. N. Ramos, B. Champagne, G. Prampolini, and F. Castet, "Temperature Effects on the Conformational Dynamics and Nonlinear Optical Properties of Donor–Acceptor Stenhouse Adducts in Chloroform Solution," *Theoretical Chemistry Accounts* 144 (2025): 65.

19. N. A. Murugan, R. Apostolov, Z. Rinkevicius, J. Kongsted, E. Lindahl, and H. Ågren, "Association Dynamics and Linear and Nonlinear Optical Properties of an N-Acetylaladanamide Probe in a POPC Membrane," *Journal of the American Chemical Society* 135 (2013): 13590–13597.

20. S. Osella, N. A. Murugan, N. K. Jena, and S. Knippenberg, "Investigation Into Biological Environments Through (Non)Linear Optics: A Multiscale Study of Laurdan Derivatives," *Journal of Chemical Theory and Computation* 12 (2016): 6169–6181.

21. C. Bouquiaux, C. Tonnelé, F. Castet, and B. Champagne, "Second-Order Nonlinear Optical Properties of an Amphiphilic Dye Embedded in a Lipid Bilayer. A Combined Molecular Dynamics-Quantum Chemistry Study," *Journal of Physical Chemistry. B* 124 (2020): 2101–2109.

22. C. Bouquiaux, F. Castet, and B. Champagne, "Unravelling the Effects of Cholesterol on the Second-Order Nonlinear Optical Responses of Di-8-ANEPPS Dye Embedded in Phosphatidylcholine Lipid Bilayers," *Journal of Physical Chemistry. B* 125 (2021): 10195–10212.

23. C. Bouquiaux, F. Castet, and B. Champagne, "Influence of the Nature of the Lipid Building Blocks on the Second-Order Nonlinear Optical Responses of an Embedded Di-8-ANEPPS Probe," *Journal of Physical Chemistry. B* 127 (2023): 528–541.

24. C. Bouquiaux, F. Castet, and B. Champagne, "Investigating the Influence of the Lipid Structure on the Global Membrane Organization: Effect of the Fatty Acids," *ChemistrySelect* 8 (2023): e202304508.

25. L. Lescos, P. Beaujean, C. Tonnelé, et al., "Self-Assembling, Structure and Nonlinear Optical Properties of Fluorescent Organic Nanoparticles in Water," *Physical Chemistry Chemical Physics* 23 (2021): 23643–23654.

26. T. N. Ramos, L. Le Bras, Y. L. Dory, and B. Champagne, "Second Harmonic Generation Signatures of Supramolecular Assemblies Based on Amide Moieties," *ChemPhysChem* 24 (2023): e202300150.

27. T. N. Ramos and B. Champagne, "Disentangling the Molecular Polarizability and First Hyperpolarizability of Methanol-Air Interfaces," *Physical Chemistry Chemical Physics* 26 (2024): 8658–8669.

28. T. N. Ramos and B. Champagne, "Modeling Second Harmonic Generation at Alcohol/Air Interfaces. A Molecular Multi-Layer Approach," *Journal of Molecular Liquids* 428 (2025): 127499.

29. M. de Wergifosse, E. Botek, E. De Meulenaere, K. Clays, and B. Champagne, "ONIOM Investigation of the Second-Order Nonlinear Optical Responses of Fluorescent Proteins," *Journal of Physical Chemistry. B* 122 (2018): 4993–5005.

30. A. Dellai, I. Krismer, G. Prampolini, B. Champagne, T. N. Ramos, and F. Castet, "Solvent Effects on the Second Harmonic Responses of Donor-Acceptor Stenhouse Adducts: From Implicit to Hybrid Solvation Models," *Physical Chemistry Chemical Physics* 27 (2025): 672–686.

31. C. Bouquiaux, P. Beaujean, T. N. Ramos, F. Castet, V. Rodriguez, and B. Champagne, "First Hyperpolarizability of the di-8-ANEPPS and DR1 Nonlinear Optical Chromophores in Solution. An Experimental and Multi-Scale Theoretical Chemistry Study," *Journal of Chemical Physics* 159 (2023): 174307.

32. S. Grimme, "A Simplified Tamm-Dancoff Density Functional Approach for the Electronic Excitation Spectra of Very Large Molecules," *Journal of Chemical Physics* 138 (2013): 244104.

33. C. Bannwarth and S. Grimme, "A Simplified Time-Dependent Density Functional Theory Approach for Electronic Ultraviolet and Circular Dichroism Spectra of Very Large Molecules," *Computational and Theoretical Chemistry* 1040–1041 (2014): 45–53.

34. M. de Wergifosse and S. Grimme, "Nonlinear-Response Properties in a Simplified Time-Dependent Density Functional Theory (sTD-DFT) Framework: Evaluation of Excited-State Absorption Spectra," *Journal of Chemical Physics* 150 (2019): 150.

35. M. de Wergifosse and S. Grimme, "Perspective on Simplified Quantum Chemistry Methods for Excited States and Response Properties," *Journal of Physical Chemistry. A* 125 (2021): 3841–3851.

36. C. Bannwarth, E. Caldeweyher, S. Ehlert, et al., "Extended Tight-Binding Quantum Chemistry Methods," *Wiley Interdisciplinary Reviews: Computational Molecular Science* 11 (2021): e1493.

37. S. Löffelsender, P. Beaujean, and M. de Wergifosse, "Simplified Quantum Chemistry Methods to Evaluate Non-Linear Optical Properties of Large Systems," *Wiley Interdisciplinary Reviews: Computational Molecular Science* 14, no. 1 (2024): e1695.

38. J. Seibert, B. Champagne, S. Grimme, and M. de Wergifosse, "Dynamic Structural Effects on the Second-Harmonic Generation of Tryptophane-Rich Peptides and Gramicidin A," *Journal of Physical Chemistry. B* 124 (2020): 2568–2578.

39. P. Beaujean, B. Champagne, S. Grimme, and M. de Wergifosse, "All-Atom Quantum Mechanical Calculation of the Second-Harmonic Generation of Fluorescent Proteins," *Journal of Physical Chemistry Letters* 12 (2021): 9684–9690.

40. M. de Wergifosse, P. Beaujean, and S. Grimme, "Ultrafast Evaluation of Two-Photon Absorption With Simplified Time-Dependent Density Functional Theory," *Journal of Physical Chemistry. A* 126 (2022): 7534–7547.

41. S. Löffelsender, M. G. Maraldi, and M. de Wergifosse, "All-Atom Quantum Mechanical Methodologies for One- and Two-Photon Absorption of Realistic Systems," *ChemPhysChem* 26 (2025): e202401121.

42. A. Dellai, C. Courdurié, S. Dubuis, et al., "Second Harmonic Responses of Clickable Azobenzenes in Solution: Comparative Hyper-Rayleigh Scattering and Density Functional Theory Studies," *Dyes and Pigments* 220 (2023): 111744.

43. R. Bersohn, Y. Pao, and H. L. Frisch, "Double-Quantum Light Scattering by Molecules," *Journal of Chemical Physics* 45 (1966): 3184–3198.

44. J. P. Bergsma, P. H. Berens, K. R. Wilson, D. R. Fredkin, and E. J. Heller, "All-Atom Quantum Mechanical Methodologies for One- and Two-Photon Absorption of Realistic Systems," *Journal of Physical Chemistry* 88 (1984): 612–619.

45. J. Cerezo, F. Santoro, and G. Prampolini, "Comparing Classical Approaches With Empirical or Quantum-Mechanically Derived Force Fields for the Simulation Electronic Lineshapes: Application to Coumarin Dyes," *Theoretical Chemistry Accounts* 135 (2016): 143.

46. H. Reis, "Problems in the Comparison of Theoretical and Experimental Hyperpolarizabilities Revisited," *Journal of Chemical Physics* 125 (2006): 014506.

47. M. de Wergifosse and S. Grimme, "Nonlinear-Response Properties in a Simplified Time-Dependent Density Functional Theory (sTD-DFT) Framework: Evaluation of the First Hyperpolarizability," *Journal of Chemical Physics* 149 (2018): 149.

48. K. Nishimoto and N. Mataga, "Electronic Structure and Spectra of Some Nitrogen Heterocycles," *Zeitschrift für Physikalische Chemie* 12 (1957): 335–338.

49. K. Ohno, "Some Remarks on the Pariser-Parr-Pople Method," *Theoretica Chimica Acta* 2 (1964): 219–227.

50. G. Klopman, "A Semiempirical Treatment of Molecular Structures. II. Molecular Terms and Application to Diatomic Molecules," *Journal of the American Chemical Society* 86 (1964): 4550–4557.

51. S. Ghosh and S. P. Bhattacharyya, "Localization in Some Discontinuously and Randomly Driven Quantum Systems," *International Journal of Quantum Chemistry* 110 (2010): 2637–2644.

52. S. Grimme and C. Bannwarth, "Ultra-Fast Computation of Electronic Spectra for Large Systems by Tight-Binding Based Simplified Tamm-Dancoff Approximation (sTDA-xTB)," *Journal of Chemical Physics* 145 (2016): 054103.

53. L. E. Johnson, L. R. Dalton, and B. H. Robinson, "Optimizing Calculations of Electronic Excitations and Relative Hyperpolarizabilities of Electrooptic Chromophores," *Accounts of Chemical Research* 47 (2014): 3258–3265.

54. L. Lescos, S. Sitkiewicz, P. Beaujean, et al., "Performance of DFT Functionals for Calculating the Second-Order Nonlinear Optical Properties of Dipolar Merocyanines," *Physical Chemistry Chemical Physics* 22 (2020): 16579–16594.

55. M. J. Frisch, G. W. Trucks, H. B. Schlegel, et al., "Gaussian 16 Revision C.01, Gaussian Inc, 2016".

56. S. Grimme, "xtb4stda version 1.0, 2019".

57. S. Grimme, "std2 version 2.0.1, 2025".

58. F. Castet and B. Champagne, "Simple Scheme to Evaluate Crystal Nonlinear Susceptibilities: Semiempirical AM1 Model Investigation of 3-Methyl-4-nitroaniline Crystal," *Journal of Physical Chemistry. A* 105 (2001): 1366–1370.

59. V. Gavini, B. Stefano, B. Volker, et al., "Roadmap on Electronic Structure Codes in the Exascale Era," *Modelling and Simulation in Materials Science and Engineering* 31 (2023): 063301.

60. M. de Wergifosse and S. Grimme, "The eXact Integral Simplified Time-Dependent Density Functional Theory (XsTD-DFT)," *Journal of Chemical Physics* 160 (2024): 204110.

61. M. de Wergifosse, "Computing Excited States of Very Large Systems With Range-Separated Hybrid Functionals and the Exact Integral Simplified Time-Dependent Density Functional Theory (XsTD-DFT)," *Journal of Physical Chemistry Letters* 15 (2024): 12628–12635.

62. M. G. Maraldi and M. de Wergifosse, "Evaluating the Performance of the Exact Integral Simplified Time-Dependent Density Functional Theory (XsTD-DFT) to Compute One- and Two-Photon Absorption," *Journal of Physical Chemistry. A* 129 (2025): 8178–8203.

Supporting Information

Additional supporting information can be found online in the Supporting Information section. **Data S1**: jcc70336-sup-0001-Supinfo.pdf. Molecular structures and NLO properties of all systems described in the text (ZIP archive); additional details on the parameterization of the sTD-DFT scheme; additional results on the impact of geometrical distortions and of intermolecular interactions on the NLO responses; static NLO properties of increasingly large AZO clusters.